Structure, magnetism, and transport of single-crystalline RNiSi$_3$ (R = Y, Gd-Tm, Lu)

Fabiana R. Arantes,[1] Deisy Aristizábal-Giraldo,[1,2] Sueli H. Masunaga,[3,4] Fanny N. Costa,[1] Fabio F. Ferreira,[1] Toshiro Takabatake,[5] Leticie Mendonça-Ferreira,[1] Raquel A. Ribeiro,[1] and Marcos A. Avila[1,*]

[1]*CCNH, Universidade Federal do ABC (UFABC), Santo André, SP, Brazil*
[2]*Instituto de Física, Universidad de Antioquia, Medellín, Colombia*
[3]*Instituto de Física, Universidade de São Paulo, Brazil*
[4]*Centro Universitário da FEI, São Bernardo do Campo, SP, Brazil*
[5]*Graduate School of Advanced Sciences of Matter, Hiroshima University, Higashi-Hiroshima, Japan*

(Received 6 December 2017; revised manuscript received 12 February 2018; published 6 April 2018)

We report on the physical properties of the intermetallic series RNiSi$_3$ (R = Y, Gd-Tm, Lu). High quality single crystals with platelike morphology were grown using the Sn flux method. X-ray powder diffraction data show that this series crystallizes in the orthorhombic space group *Cmmm*, and Laue patterns indicate that the **b** axis remains perpendicular to the plane of the plates. Magnetization measurements show anisotropic antiferromagnetic ground states for R = Gd-Tm with Néel temperatures ranging from T_N = 2.6 K (TmNiSi$_3$) up to 32.2 K (TbNiSi$_3$), as well as metamagnetic transitions that in some cases appear together with hysteresis (TbNiSi$_3$, DyNiSi$_3$, and HoNiSi$_3$). The easy axis changes from **a** axis to **b** axis on going from R = Gd-Ho to R = Er-Tm. All transitions from antiferromagnetic to paramagnetic states are clearly marked by sharp peaks in specific heat as well as in the derivative of resistivity measurements, which show metallic temperature dependence for all compounds and residual values in the range of 1 $\mu\Omega$ cm. DyNiSi$_3$ has two close phase transitions, while HoNiSi$_3$ presents distinct critical temperatures for applied fields in the a or c directions (10.4 and 6.3 K, respectively), pointing to possible component-specific ordering of the local magnetic moments.

DOI: 10.1103/PhysRevMaterials.2.044402

I. INTRODUCTION

Intermetallic compounds based on rare earth and 3d transition elements display a rich variety of peculiar phenomena, including complex magnetic structures [1,2], non-Fermi liquid behavior [3,4], quantum criticality [5,6], and even unconventional superconductivity [7].

Magnetic properties of many such compounds are strongly influenced by magnetic contributions from a 3d transition metal, such as in Mn-based systems [8,9], in addition to the rare earth magnetic moment. The concomitant magnetism between the 3d and 4f electrons typically display high magnetic ordering temperatures and often a prevalence of the exchange coupling between the 3d atoms on the magnetic properties. There are, however, compounds where the transition metal atom does not carry any magnetic moment, as in the case of Ni in the parent germanide series, RNiGe$_3$ (R = rare earth) [10]. The lack of magnetic moment of Ni is due to its completely filled metallic 3d band, presumably via dsp^2 hybridization. Another example is the series RFe$_2$Ge$_2$ where, for most compounds, the Fe atoms do not seem to bear any magnetic moment, although LuFe$_2$Ge$_2$ shows an anomaly in specific heat, magnetic susceptibility, and resistivity measurements at 9 K possibly associated with a long range antiferromagnetic order of Fe atoms [11–14].

For systems with pure 4f magnetism, the long-range Ruderman-Kittel-Kasuya-Yosida (RKKY) interaction between the rare earths and their sensitivity to the crystal electric field (CEF), play a major role in the rich variety of their magnetic structures [15,16]. The compounds in the germanide series (RNiGe$_3$) have already been well characterized, showing antiferromagnetic (AFM) ground states with strong axial anisotropy and a marked influence of CEF effects on the magnetic properties [10,17]. Among these, CeNiGe$_3$ has drawn attention for showing unconventional superconductivity below 0.48 K and under pressure [18,19], while YbNiGe$_3$ stands out for showing a pressure-induced shift in the valence of the Yb atoms through a quantum critical point [20,21].

In contrast, the basic physical properties of the silicide series (RNiSi$_3$) have so far remained virtually unexplored, thus being the aim of this work. A 1977 study was the first to report on the existence of the RNiSi$_3$ compounds, and indicated paramagnetic behavior between 80 and 1200 K for polycrystalline samples [22]. The crystal structures in this series were later determined for SmNiSi$_3$ [23] and ErNiSi$_3$ [24], in both cases crystallizing in the orthorhombic space group *Cmmm*, the same for most of the RNiGe$_3$ series. The only compound of the RNiSi$_3$ series that has been fully characterized is YbNiSi$_3$, in which single-crystalline samples revealed an AFM Kondo lattice ground state, showing a relatively high Néel temperature T_N = 5.1 K, with an easy AFM axis along the orthorhombic **b** axis [25–27]. The determination of the magnetic structure of this compound by neutron scattering showed that the Yb magnetic moments have a ferromagnetic (FM) alignment along the bc plane, which stacks antiferromagnetically along the **a** axis [28]. Our preliminary work [29] showed the growth of single-crystalline DyNiSi$_3$ and HoNiSi$_3$, with the samples displaying complex AFM behavior.

*avila@ufabc.edu.br

In this work we have expanded the exploration to the full series of RNiSi$_3$, having succeeded in growing single crystals of the family with R = Y, Gd-Tm, Lu and characterized them using x-ray diffraction, magnetic susceptibility, heat capacity, and resistivity measurements.

II. EXPERIMENTAL METHODS

Single crystals of the series RNiSi$_3$ (R = Y, Gd-Tm, Lu) were obtained using the Sn flux method with a quaternary molar proportion of 1:1:3:45 (R:Ni:Si:Sn). Elemental reagents were supplied by Alfa Aesar with purities of 99.95% for Ni, 99.999% for Si and Sn, and 99.9% for all the rare earths except for Y, which was supplied by Ames Laboratory and is of higher purity. The samples were grown by sealing the elements inside evacuated quartz ampoules, which were then placed in a box furnace. The ampoules were heated from room temperature up to 1200 °C, a temperature under which all the elements of the mixture are melted over several hours, and then slowly cooled down to 500 °C over 150 h to allow the single crystals to nucleate and grow. At 500 °C the ampoules were removed from the furnace and centrifuged in order to separate the crystals from the flux. After opening the ampoules, selected crystals were then cleaned in HCl to remove residual Sn droplets.

The crystal structures were evaluated by x-ray powder diffraction in a Stoe diffractometer, model STADI P, with Cu$K_{\alpha 1}$ radiation and at room temperature. The single crystals were hand-ground in an agate mortar with pestle and the powder was then loaded between two acetate-cellulose foils, which were kept spinning during measurement. Additional platelike single crystals were oriented by the Laue method. Magnetization measurements were obtained in a Quantum Design MPMS3 SQUID-VSM, in the temperature range between 1.8 and 300 K, and under external applied fields of up to 70 kOe. Some of the samples (TbNiSi$_3$, DyNiSi$_3$, and HoNiSi$_3$) showed hysteretic behavior, so special care was taken to always demagnetize the samples with an oscillating magnetic field and to warm them above their Néel temperatures before each new measurement. The magnetic responses of the samples were studied along the three principal crystallographic directions, **a**, **b**, and **c**. Specific heat measurements were conducted in a Quantum Design PPMS DynaCool system at zero field with the thermal-relaxation technique between 2 and 50 K. The resistivity measurements were taken in the same PPMS, with the standard four probe geometry, both with no field and under an applied field of 90 kOe, for temperatures between 2 and 300 K, and in samples with typical thickness of 0.2 mm, width of about 0.6 mm, and length between 0.8 mm and a few millimeters.

III. MORPHOLOGY AND CRYSTAL STRUCTURE

The single crystals of this series grow with a thin platelike geometry, as exemplified in Fig. 1 for a DyNiSi$_3$ sample, with well-defined and shiny surfaces. Laue diffraction patterns indicated that the **b** axis remains perpendicular to the plane of the plates, while the visual determination of the axes **a** and **c** is not clear. This platelike geometry, with the **b** axis perpendicular to the plane, was also reported for YbNiSi$_3$ [25] and for the RNiGe$_3$ family [10]. For each synthesis, several high quality single crystals were obtained; however, particularly for ErNiSi$_3$, TmNiSi$_3$, and LuNiSi$_3$, special care was needed due to the presence of small parasitic-phase crystallites on the crystal surfaces that had to be removed for the measurements (Fig. 1). Several attempts were made to obtain the other unreported compounds in this family (R = La-Nd, Sm, and Eu) but none yielded the desired phase through the Sn flux method.

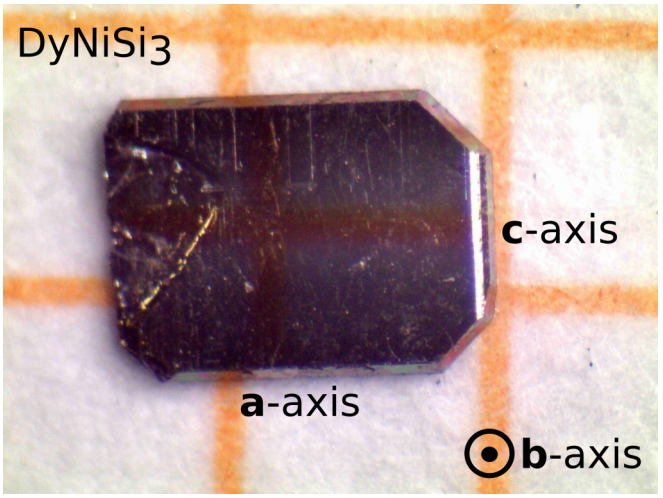

FIG. 1. Picture of a single-crystalline DyNiSi$_3$ sample displaying platelike morphology, over millimeter paper. The **a**, **b**, and **c** crystallographic axes determined from Laue patterns for this crystal are indicated. The scale of the grid is 1 mm.

The Rietveld refinement of GdNiSi$_3$ (representative of typical patterns observed for the RNiSi$_3$ family) using x-ray powder diffraction data (Fig. 2) shows that the crystal adopts the SmNiGe$_3$-type orthorhombic lattice and $Cmmm$ space

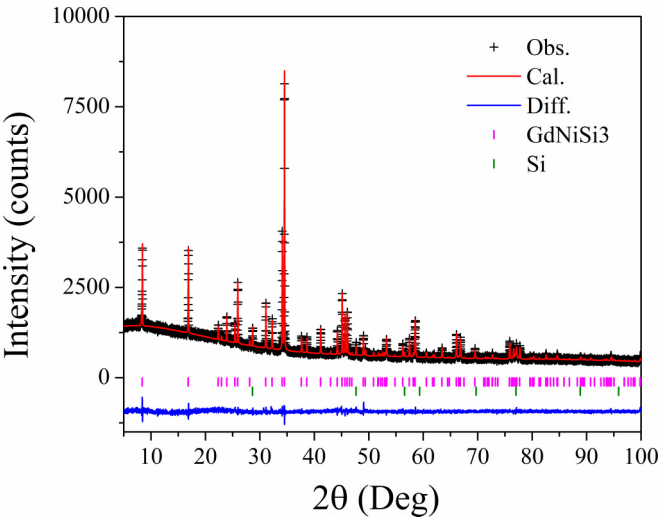

FIG. 2. Rietveld plot for GdNiSi$_3$ as a representative pattern obtained for the RNiSi$_3$ series. The black crosses represent observed data, the red line indicates the calculated pattern, and the blue line at the bottom represents the difference between the observed and calculated patterns. The vertical bars indicate Bragg reflections of each identified phase.

TABLE I. Lattice parameters and unit cell volumes with their respective estimated standard deviations (in parentheses) obtained from the Rietveld refinements for each compound of the RNiSi$_3$ series. The R factors and the goodness of fit are also displayed in the table. The values for YbNiSi$_3$ were obtained from Ref. [25].

Compound	a (Å)	b (Å)	c (Å)	V (Å^3)	R_{wp} (%)	χ^2 (%)	R_{Bragg} (%)
YNiSi$_3$	3.9216(1)	20.9448(6)	3.9506(1)	324.49(2)	14.492	2.744	8.157
GdNiSi$_3$	3.9402(2)	21.0224(6)	3.9730(1)	329.10(2)	3.901	1.042	0.869
TbNiSi$_3$	3.9259(1)	20.9696(5)	3.9547(1)	325.57(1)	4.629	1.073	1.706
DyNiSi$_3$	3.9167(2)	20.929(1)	3.9401(2)	322.98(3)	4.652	1.004	1.593
HoNiSi$_3$	3.9085(1)	20.9057(4)	3.92915(9)	321.05(1)	8.532	1.429	3.859
ErNiSi$_3$	3.9015(1)	20.8817(6)	3.9181(1)	319.21(2)	17.120	3.519	10.618
TmNiSi$_3$	3.89301(8)	20.8417(4)	3.90578(7)	316.90(1)	11.228	2.009	5.339
YbNiSi$_3$	3.8915(1)	20.8570(6)	3.9004(1)	316.58	–	–	–
LuNiSi$_3$	3.8808(3)	20.792(1)	3.8868(3)	313.62(4)	27.372	4.759	9.935

group, with 20 atoms in the unit cell (see Fig. 3), as reported for ErNiSi$_3$ [24] and YbNiSi$_3$ [25]. For the other samples, we found some Bragg reflections due to the Sn flux as well as an unknown phase. Further details about the Rietveld refinement for all other samples of the series can be found in the Appendix. Table I shows the lattice parameters, unit cell volumes, and some statistical factors, which can indicate the quality of the fits, obtained from the refinements for each compound. Figure 4 shows the dependence on the (a) a/c and (b) a/b ratios along the series. These data evidence that the a/c ratio is close to unity, so the structure orthorhombicity is small, and the trend shows that the series becomes almost tetragonal when advancing towards the heaviest rare earths. On the other hand, the a/b ratio [Fig. 4(b)] decreases along the series, indicating that the unit cell becomes more elongated for the heaviest compounds. It should be noticed that indications of small

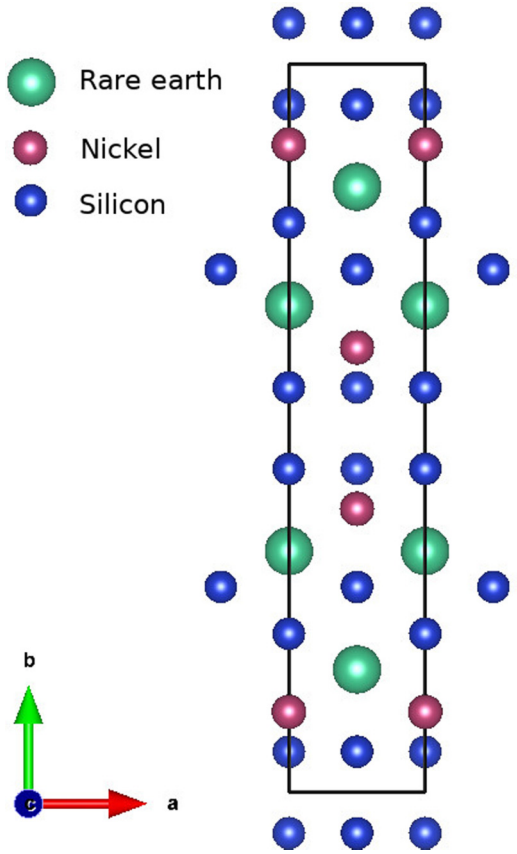

FIG. 3. Crystal structure of the RNiSi$_3$ series along the crystal ab plane. The solid black line indicates the unit cell.

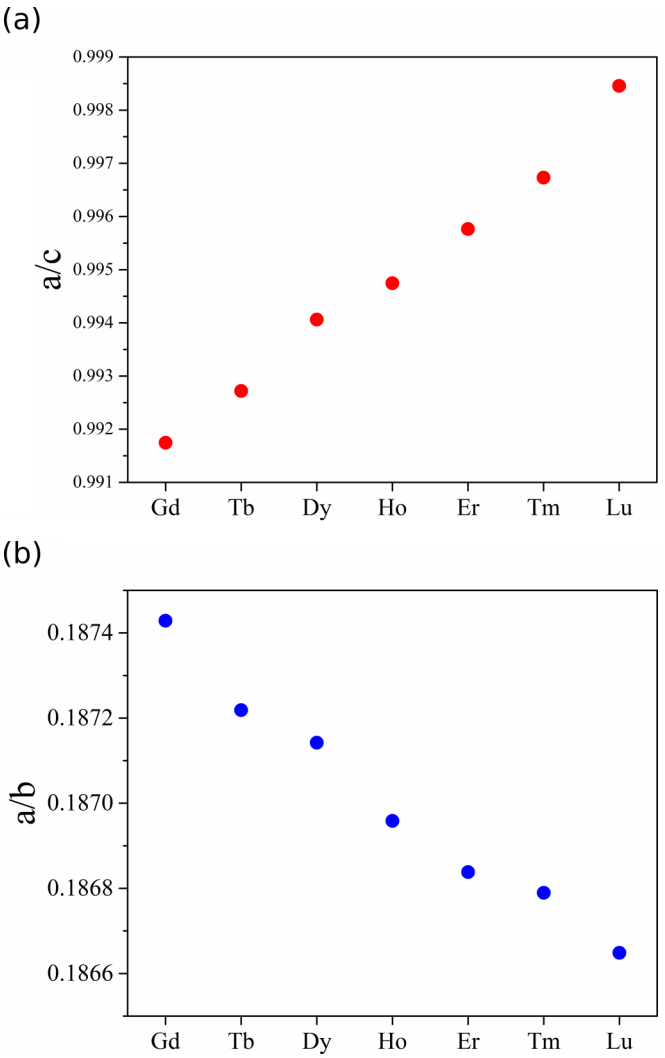

FIG. 4. Lattice parameter ratios (a) a/c and (b) a/b along the RNiSi$_3$ series.

amounts of Sn due to the flux and an unknown phase are present in all x-ray patterns, especially for $ErNiSi_3$, but they were not considered in the Rietveld refinements.

IV. PHYSICAL PROPERTIES

All compounds of the RNiSi$_3$ series present anisotropic magnetic behavior, with the presence of an AFM ground state for $GdNiSi_3$ up to $TmNiSi_3$. For the latter, the magnetization curves are marked by metamagnetic transitions, displaying an easy axis along the **a** crystallographic axis for R = Gd-Ho, and a shift to the **b** axis for $ErNiSi_3$ and $TmNiSi_3$. $YNiSi_3$ and $LuNiSi_3$, on the other hand, show paramagnetic or diamagnetic responses, depending on the direction of the applied field.

The Néel temperature of AFM systems can be obtained directly from the anomaly seen in the specific heat due to the magnetic transition. Also, the magnetic specific heat (C_m) is proportional to the derivative of the susceptibility (χ), as expressed by the relation $C_m \simeq A\partial[T\chi(T)]/\partial T$, where A has only a weak dependence on T [30], which turns $\chi(T)$ measurements into an independent way of estimating T_N. Additionally, resistivity measurements are usually sensitive to changes in the magnetic phase transitions due to the effect of the spin ordering on the scattering of conduction electrons [31,32].

For the compounds of the RNiSi$_3$ series displaying magnetic ordering (R = Gd-Tm) we have used these three techniques to observe the transition from the AFM to the paramagnetic state. Figure 5 exemplifies the procedure to determine the transition temperatures using the results for $GdNiSi_3$, where the dashed black line denotes the average T_N obtained from the three measurements.

In Fig. 5(a) the peak at 22.2 K clearly determines the transition from the paramagnetic to the AFM state; however in the resistivity measurement, shown in Fig. 5(b), the temperature where the transition takes place is not so evident. For the $\rho(T)$ curves in all samples, the transition temperature was estimated using a linear segmented regression where its breakpoint gives T_N [33,34]. This amounts to fitting a function composed of two contiguous segments to the points close to the transition:

$$\rho(T) = \begin{cases} a + bT, \text{ for } T \leqslant T_N, \\ a + bT + c(T - T_N), \text{ for } T > T_N, \end{cases} \quad (1)$$

where a, b, c, and T_N are free parameters. This function allows us to extract where the behavior of the curve changes and, although it has no theoretical basis, it provides a sufficiently accurate value of T_N. Some authors use the maximum of the derivative curve $d\rho(T)/dT$; however this is somewhat inaccurate, especially for samples like ours that show very low resistivity resulting in experimental data often at the limit of the equipment resolution.

Figure 5(c) displays the susceptibility curves, with the field applied along the three crystallographic axes, and their resulting estimated "polycrystalline average" susceptibility curve as a continuous black line. The average curve was computed as the arithmetic mean of the susceptibilities measured in the three main crystallographic directions at each temperature. Both zero field cooled (ZFC) and field cooling (FC) measurements were performed under 1000 Oe for all samples, yielding the same results, i.e., there was no thermal hysteresis. For clarity we show only the FC curves in the subsequent results section.

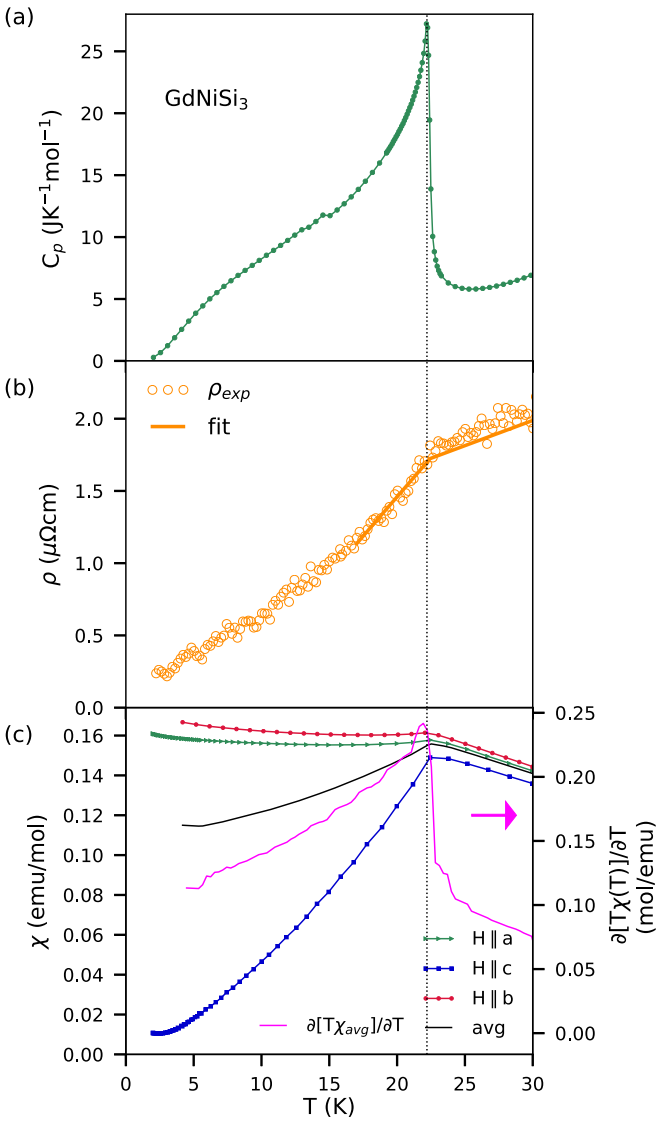

FIG. 5. Determination of the Néel temperature for $GdNiSi_3$ from (a) specific heat, (b) resistivity, and (c) magnetic susceptibility measurements. The dashed line indicates the average Néel temperature obtained from the three measurements.

As explained above, T_N in this case can be determined by the peak of the $\partial[T\chi(T)]/\partial T$ curve (magenta line, right axis). The Néel temperatures obtained from the three techniques have an excellent agreement with an average value of T_N = 22.2(2) K for $GdNiSi_3$.

The transition temperatures for all compounds presenting magnetic order are shown in Table II. $DyNiSi_3$ and $HoNiSi_3$ display two transitions, and the highest temperature is taken as T_N, since in both compounds this is the critical temperature of the ordering along the easy AFM axis (**a** crystallographic axis). In the Appendix we present the correspondents of Fig. 5 for all the remaining compounds.

The following subsections detail the characteristics specific to each compound, beginning from $YNiSi_3$ and $LuNiSi_3$ and then proceeding up to $TmNiSi_3$.

TABLE II. Néel temperatures. Each entry corresponds to the value of T_N obtained from either the specific heat (C_p), resistivity (ρ), or magnetic susceptibility (χ), while the last column averages over the previous three values.

R	C_p (K)	ρ (K)	χ (K)	Average (K)
Gd	22.2	22.4	21.9	22.2(2)
Tb	33.0	33.4	33.3	33.2(2)
Dy[a]	22.8, 23.6	21.8	22.7, 23.6	22.8(2), 23.6(2)
Ho[a]	6.3, 10.1	10.7	6.3, 10.4	6.3(2), 10.4(3)
Er	3.7	3.6	3.7	3.7(1)
Tm	2.6	2.7	2.6	2.6(1)

[a]It was not possible to determine the two transitions from the resistivity measurements for $DyNiSi_3$ and $HoNiSi_3$, so in the average value displayed in the last column those data were not taken into account for $DyNiSi_3$ and only the highest value for $HoNiSi_3$.

A. $YNiSi_3$ and $LuNiSi_3$

For $YNiSi_3$ and $LuNiSi_3$ the rare earths Y and Lu do not carry a magnetic moment, so they can be used as a nonmagnetic reference for the remaining compounds of the series. It is especially important for the magnetic measurements, where we can confirm whether or not the magnetic response includes contributions from the Ni atoms.

In order to evaluate the magnetic specific heat for the magnetic compounds of this series and to calculate the entropy related to their phase transitions, it is necessary to subtract the nonmagnetic contributions of the lattice, the electrons, and, sometimes, higher order terms. Usually this can be done measuring the specific heat of analogous nonmagnetic compounds and then subtracting this from the specific heat of the magnetic compound of interest [35]. Figure 6(a) shows the dependence of the specific heat on the temperature for $YNiSi_3$ and $LuNiSi_3$, and the same data, plotted as C_p/T vs T^2, is displayed in the inset with the best fit obtained using the Debye model $C_p(T) = \gamma T + AT^3$, where γ is the Sommerfeld coefficient, for the data up to ≈ 12 K. C_p for both compounds exhibit a smooth dependence on T, and there is no evidence of any phase transitions in the measured temperature range. The inset shows that the linear fit can describe the data accurately at low temperatures and yields an estimated Debye temperature θ_D of 393 K for $YNiSi_3$ ($A = 0.160$ mJ K^{-4} mol^{-1}) and 489 K for $LuNiSi_3$ ($A = 0.0830$ mJ K^{-4} mol^{-1}). The values obtained for γ, related to the electronic contribution for C_p, are 4.1 and 3.5 mJ K^{-1} mol^{-1} for $YNiSi_3$ and $LuNiSi_3$, respectively.

In the data presented in the following sections, the subtraction of the nonmagnetic contribution using the data displayed in Fig. 6(a) was done using a similar procedure described in Ref. [11]. Instead of fitting the results with a polynomial, we directly subtracted an interpolation of the experimental points, averaging the contribution of $YNiSi_3$ and $LuNiSi_3$ through an expression based on the Debye expansion [11,36]:

$$C_{nm}^{(R)}(T) = C_p^{(\mathrm{Lu})}(T) - \left[C_p^{(\mathrm{Lu})}(T) - C_p^{(\mathrm{Y})}(T)\right] \times \frac{\left(M_{\mathrm{Lu}}^{3/2} - M_R^{3/2}\right)}{M_{\mathrm{Lu}}^{3/2} - M_{\mathrm{Y}}^{3/2}}, \quad (2)$$

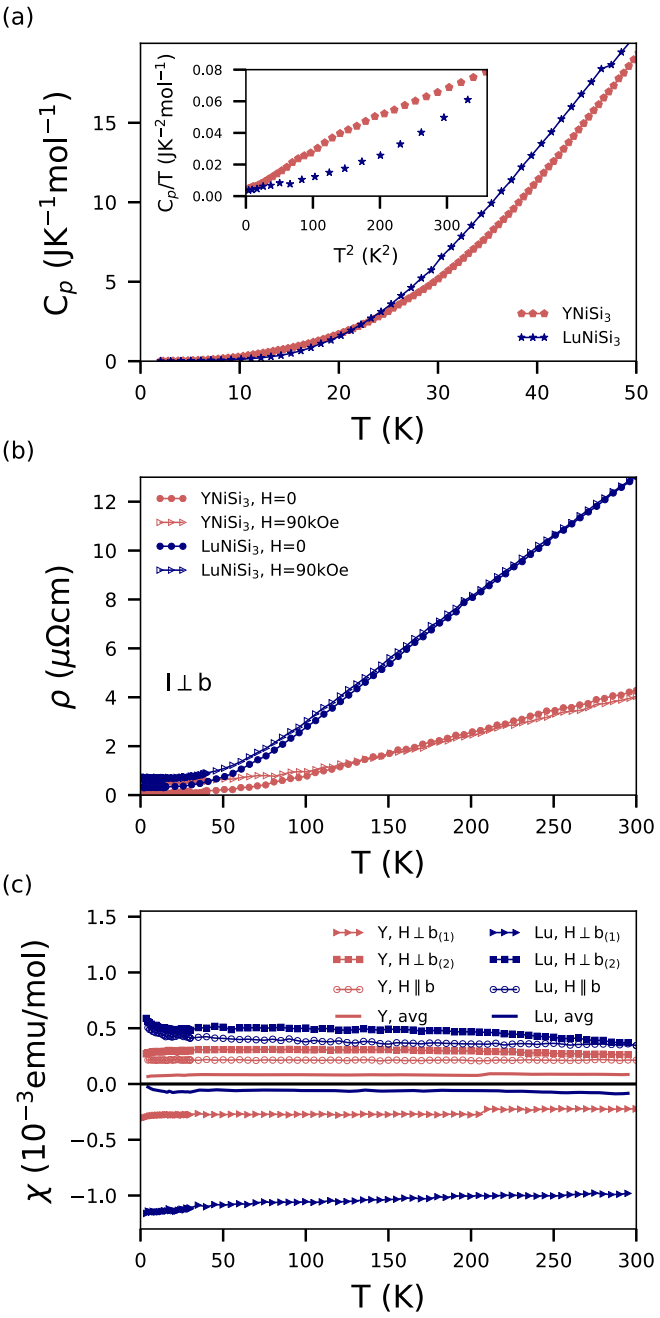

FIG. 6. Physical properties of $YNiSi_3$ and $LuNiSi_3$. (a) Dependence of the specific heat on the temperature, with the best Debye model fit in the inset using the $C_p/T \times T^2$ curves. (b) Dependence of resistivity on the temperature with no field (solid symbols) and with an applied field of 90 kOe (open symbols). (c) Susceptibility curves with an applied field of $H = 1000$ Oe parallel to the three crystallographic axes. The average curve for both samples are presented as a solid line.

where $C_{nm}^{(R)}(T)$ is the nonmagnetic specific heat of the compound of the respective rare earth R, $C_p^{(\mathrm{Y})}(T)$ and $C_p^{(\mathrm{Lu})}(T)$ are the specific heat related to $YNiSi_3$ and $LuNiSi_3$, respectively, and M_X is the molar mass of each atom. It is worthy to note that, at low temperatures, the phonon contribution of $YNiSi_3$ is larger than of $LuNiSi_3$ [inset Fig. 6(a)], so Eq. (2) is not accurate at this temperature range. The same behavior was

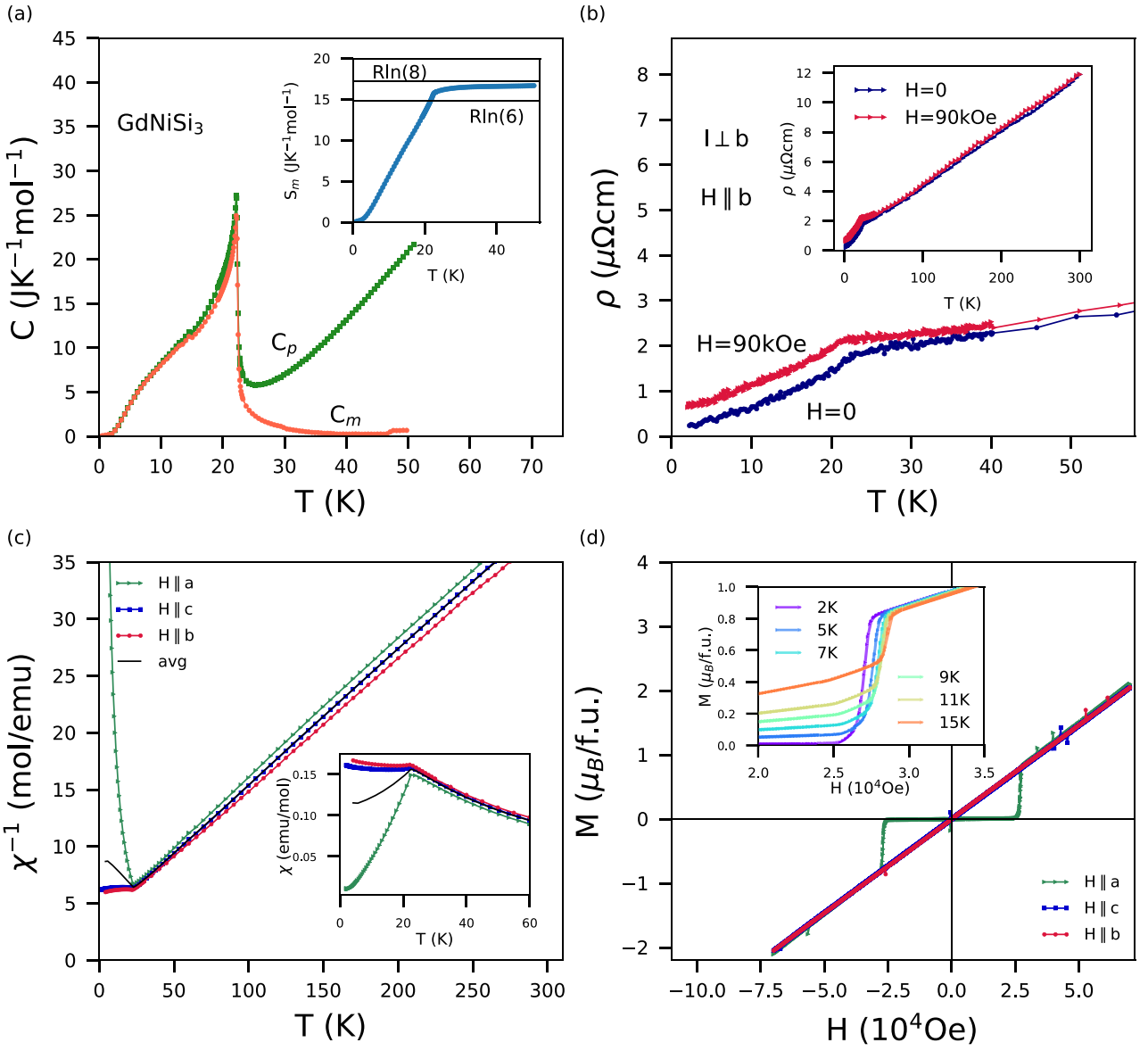

FIG. 7. Physical characterization of $GdNiSi_3$. (a) Total (C_p) and magnetic (C_m) zero-field specific heat curves. The inset portrays the released magnetic entropy. (b) Resistivity measured under zero field and 90 kOe in the temperature range where the AFM transition takes place. The inset shows the full zero-field curve up to room temperature. (c) Inverse magnetic susceptibility χ^{-1} under $H = 1000$ Oe along the **a**, **b**, and **c** axes from 2 to 300 K. The inset shows $\chi(T)$ near the magnetic transition. (d) Magnetization isotherms at 2 K in the same three directions. The inset portrays the shift of the metamagnetic transition to higher fields with increasing temperature.

also observed in the $R NiGe_3$ series, which can be due to the important Ni vacancy as detected in $LuNiGe_3$ [10].

The resistivity data for both compounds, in zero field and under an applied field of $H = 90$ kOe, are presented in Fig. 6(b), with the curves presenting metallic behavior and no visible phase transition. The residual resistivity ratios (RRR), defined as $RRR = \rho(300\ K)/\rho(2\ K)$, are equal to 54(5) for $YNiSi_3$ and 38(4) for $LuNiSi_3$, indicating high quality single crystals. Because of the small resistivity at low temperatures, the voltage signal was in the limit of the PPMS reading. Compared to their germanide counterparts, the present silicides have $\rho(T)$ an order of magnitude smaller.

The susceptibility curves as a function of temperature are displayed in Fig. 6(c), with marked anisotropic behavior for both compounds. The measurements were performed with the applied field of $H = 1000$ Oe parallel to the three crystallographic axes **a**, **b**, and **c**; however the distinction between the axes **a** and **c** was not possible, so we labeled these two directions as $\perp b_{(1)}$ and $\perp b_{(2)}$. $YNiSi_3$ presents an almost constant Pauli susceptibility (continuous magenta line) of $0.08(5) \times 10^{-3}$ emu/mol. For $LuNiSi_3$ at low temperatures there is a weak Curie-like susceptibility that can be associated with the presence of a small amount of paramagnetic impurities, since the elemental Lu reagent used was not as pure as Y. The average susceptibility for this compound (continuous blue line) is negative and, at high temperatures, equal to $-0.07(5) \times 10^{-3}$ emu/mol. For both samples the susceptibility along two directions ($\parallel b$ and $\perp b_{(2)}$) are positive, while the measurement $\perp b_{(1)}$ is negative. The presence of a negative or positive susceptibility, depending

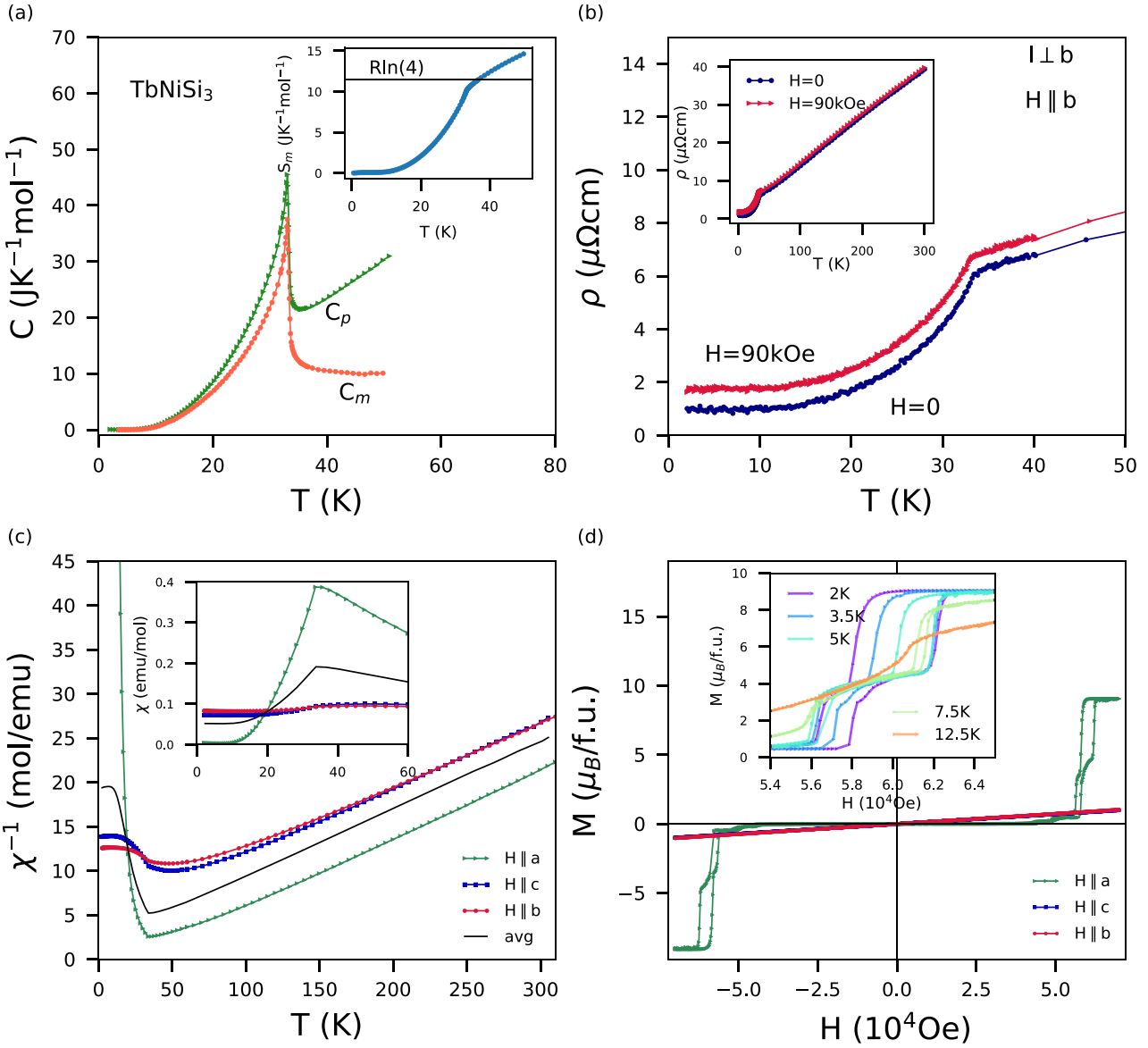

FIG. 8. Physical characterization of $TbNiSi_3$. (a) Total (C_p) and magnetic (C_m) zero-field specific heat curves. The inset shows the released magnetic entropy. (b) Zero-field resistivity from 2 to 300 K. (c) Inverse magnetic susceptibility χ^{-1} under $H = 1000$ Oe along the **a**, **b**, and **c** axes from 2 to 300 K. The inset shows $\chi(T)$ near the magnetic transition. (d) Magnetization isotherms at 2 K in the same three directions. The inset portrays the attenuation of the metamagnetic hysteresis with increasing temperature.

on the direction of the applied field, was also observed for $YNiGe_3$ [10].

B. $GdNiSi_3$

Gd-based compounds are usually characterized by low magnetic anisotropy due to their ground states with half-filled, spherical $4f$ shells ($S = 7/2$ and $L = 0$), i.e., at first order they are usually insensitive to the crystal electric field. Anisotropic effects in such compounds, with an AFM or FM ordering, can arise mainly as a consequence of dipolar interactions [37], although there is some discussion on the role of exchange anisotropy [38]. In rare earth compound series such as the one presented in this work, the Gd-based sample can be used as reference for studying the magnetic exchange interactions, due to lack of magnetocrystalline effects.

$GdNiSi_3$ presents an anisotropic AFM ground state ordered along the **a** crystallographic axis and with an average Néel temperature of $T_N = 22.2(2)$ K, determined using the measurements of $C_p(T)$, $\rho(T)$, and $\chi(T)$ shown in Fig. 5. Figure 7 shows the full physical characterization performed for this compound.

The dependence of the total specific heat C_p on the temperature [Fig. 7(a)] shows a sharp peak near 22 K that marks the transition between the AFM and the paramagnetic phases. The magnetic specific heat C_m was evaluated using the method described in the previous section and reaches zero at 40 K.

The molar magnetic entropy S_m, shown in the inset, was obtained by numerical integration of the C_m/T curve. A linear extrapolation from the point at the lower temperature until zero was made to minimize the error introduced by the lack of those data points. In systems where the magnetism

comes solely from the $4f$ rare ions, the magnetic entropy should reach its maximum value $R\ln(2J+1)$, where R is the gas constant, at high temperatures, when all $2J+1$ levels are populated. In Gd compounds those levels are degenerate, except in the presence of an internal magnetic field due to exchange interactions, and the magnetic specific heat is related to the changes in the magnetically ordered state [36]. For $GdNiSi_3$, the specific heat has a broad shoulder below 10 K that has been observed for other Gd-based compounds [11] and attributed to a Zeeman split due to the internal fields. The magnetic entropy almost reaches its expected value $R\ln(8)$ above the magnetic transition, as shown in the inset.

The dependence of the resistivity on the temperature is shown in Fig. 7(b), where the magnetic transition can be observed in both curves (with and without an applied magnetic field). Below the Néel temperature there is a marked decrease in $\rho(T)$, with the measurement under an applied field featuring a higher resistivity (positive magnetoresistance). This behavior was observed in antiferromagnetic materials with H parallel to the AFM axis, since the applied magnetic field may not suppress all the spin fluctuations that scatter the conduction electrons [39]. The inset shows both curves up to room temperature, where the resistivity follows T-linear behavior.

The susceptibility data [Fig. 7(c)] show that the AFM ordered moments align along the **a** axis. Below T_N, χ (inset) measured along **a** vanishes. This is associated with the increase in effectiveness of the AFM coupling and decreasing thermal fluctuations. At low temperatures, the relatively small field used to perform the measurement, 1000 Oe, has little effect on the AFM ordering and the magnetization is close to zero. However, as the temperature is increased up to T_N, the field is able to raise the magnetization. The measurements of χ perpendicular to the AFM axis, in this case parallel to the **b** and **c** axes, show little temperature dependence below T_N. In the paramagnetic state, above T_N, the magnetic response is essentially isotropic and χ decreases with increasing T, as expected. The inverse of the calculated polycrystalline average susceptibility [black line in the main graph of Fig. 7(c)] can be fitted by the Curie-Weiss law $\chi = C/(T-\theta_p)+\chi_0$ at high temperatures, which yields $\theta_p = -30(3)$ K and an effective magnetic moment of $\mu_{\rm eff} = 8.1(2)\,\mu_B$. This is consistent with the expected value for Gd^{3+} free ions, $7.94\,\mu_B$ [40].

In Fig. 7(d) we plot the magnetization as a function of the applied field. For the measurement along the **a** axis, the curve shows an initial plateau followed by a magnetic transition at 27 kOe, reaching a magnetization value of $0.82\,\mu_B$. Above the critical field the three curves follow the same trend, but until 70 kOe the compound is still far from the saturation value. Similar behavior was observed for $GdNiGe_3$ [10]. In the inset, the magnetization parallel to the **a** axis are shown for several temperatures. It is noteworthy that the critical field *increases* with the temperature, contrary to the expectations of spin-flop transitions in antiferromagnets.

C. $TbNiSi_3$

In other AFM intermetallic families, the Tb-based compounds usually show strong magnetic anisotropy with a high Néel temperature and metamagnetic transitions that can be accompanied by hysteresis [41,42]. For $TbNiGe_3$ [10], the Néel

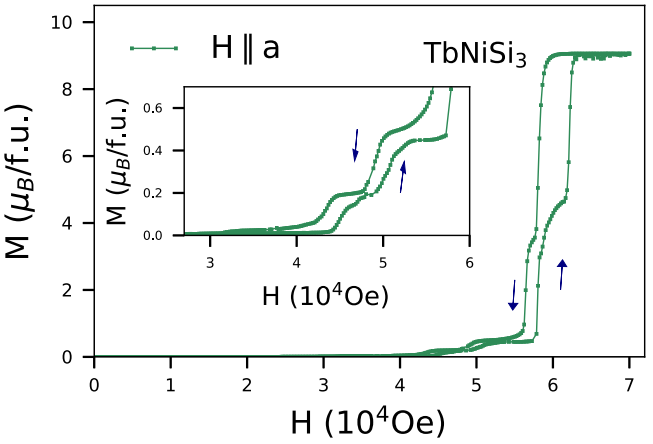

FIG. 9. Several metamagnetic transitions in the compound $TbNiSi_3$ at 2 K. The inset shows the zoom in the region of lower fields with the first transitions appearing with a critical field of $H_c = 4.3\times10^4$ Oe.

temperature is higher still than for the Gd-based compound, showing a deviation from the scaling with the de Gennes factor [40]. This behavior, according to the authors, is explained by the combination of the RKKY interaction and the crystal electric field effect. $TbNiSi_3$ exhibits the same effect, since its $T_N = 33.2(2)$ K, is higher than for $GdNiSi_3$. Figure 8 shows the physical characterization performed for $TbNiSi_3$ and more details in the evaluation of the T_N can be seen in Fig. 25 in Appendix B.

The total and magnetic specific heat [Fig. 8(a)] show a single marked peak around 33 K due to the transition from the AFM to the paramagnetic state. The magnetic entropy (inset graph) reaches a value near $R\ln(4)$ at the transition and, therefore, should be associated with four low energy levels.

Figure 8(b) shows the dependence of the resistivity on the temperature in zero field and with $H = 90$ kOe. In both curves the AFM transition is clearly seen at around 32 K, above which T-linear behavior is seen. Positive magnetoresistance is observed, as for $GdNiSi_3$.

$TbNiSi_3$ shows a well-defined AFM ordering along the **a** crystallographic axis, but similar magnetic responses appear along the axes **b** and **c** in the ordered phase. This behavior is shown both in the curve with the dependence of the susceptibility on the temperature [Fig. 8(c)] as well as in the magnetization as a function of the applied field [Fig. 8(d)]. The fit of the Curie-Weiss law for the inverse of the susceptibility gives $\mu_{\rm eff} = 9.6(3)\,\mu_B$, in agreement with the theoretical value of $9.72\,\mu_B$ [40], and $\theta_p = -8.0(8)$ K, that evidences the AFM interaction.

The most exotic feature of $TbNiSi_3$ appears in the $M(H)$ curve measured in the direction of the AFM axis **a**, shown in Fig. 8(d). The dependence of the magnetization on the applied field at low temperatures is characterized by several metamagnetic transitions accompanied by hystereses that can reach a width of 4000 Oe in the curve measured at 2 K. The inset graph displays the attenuation of this irreversible behavior with increasing temperature, while Fig. 9 shows in detail the 2 K magnetization isotherm, featuring four plateaus before the magnetic response saturates, and a closer view of the metamagnetic transitions at lower fields shown in the inset. Such sequences of multiple steps have been observed as well in, for instance, $TbNi_2Ge_2$ and $TbPd_2P_2$ [1,41], although a

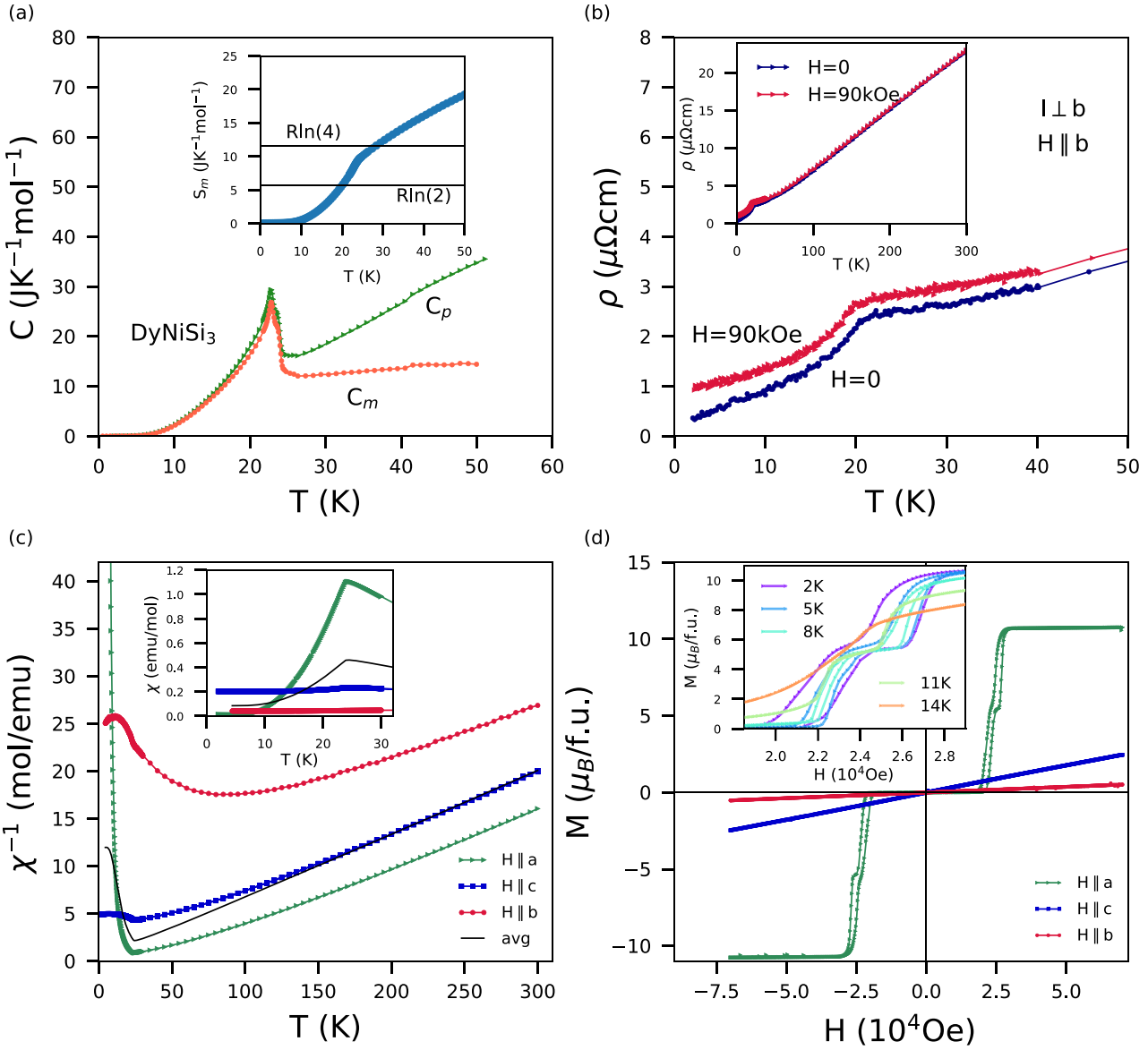

FIG. 10. Physical characterization of $DyNiSi_3$. (a) Total (C_p) and magnetic (C_m) zero-field specific heat curves. The inset portrays the released magnetic entropy. (b) Resistivity measured under zero field and 90 kOe in the temperature range where the AFM transition takes place. The inset shows the full zero-field curve up to room temperature. (c) Inverse magnetic susceptibility χ^{-1} under $H = 1000$ Oe along the **a**, **b**, and **c** axes from 2 to 300 K. The inset shows $\chi(T)$ near the magnetic transition. (d) Magnetization isotherms at 2 K in the same three directions. The inset features the isotherms highlighting the hysteretic behavior at the metamagnetic transition and its plateau.

simpler magnetic behavior was found in the related compound $TbNiGe_3$ [10].

As the lattice parameters of $TbNiSi_3$ are smaller than those of $TbNiGe_3$, the crystal field parameters can vary significantly allowing those much more complex features observed for $TbNiSi_3$. On the other hand, the presence of hysteresis possibly indicates a ferromagnetic component that may have originated from vacancies, as observed in the germanide series, where nickel vacancies were found among all compounds [10].

The complex magnetic behavior of $TbNiSi_3$ presented in this section makes it a good candidate for further studies using neutron diffraction to evaluate the several magnetic structures attained by the Tb^{3+} ions.

D. $DyNiSi_3$

The following compound of the series $DyNiSi_3$ is marked by two close transitions at 22.8(2) K and $T_N = 23.6(2)$ K, the latter being the Néel temperature. Details on the evaluation of both transitions are given in Fig. 26 in Appendix B.

Figure 10 shows the full physical characterization performed for this compound. Specific heat [Fig. 10(a)] shows a shoulder followed by a kink at 22.8(2) K from the second magnetic transition taking place at a temperature too close to the previous one to allow a better resolution of the two distinct transitions. The released magnetic entropy (inset graph) is about R ln(4) at the AFM transition, similar to other Dy-based compounds [10,11,43], although the subtracted nonmagnetic

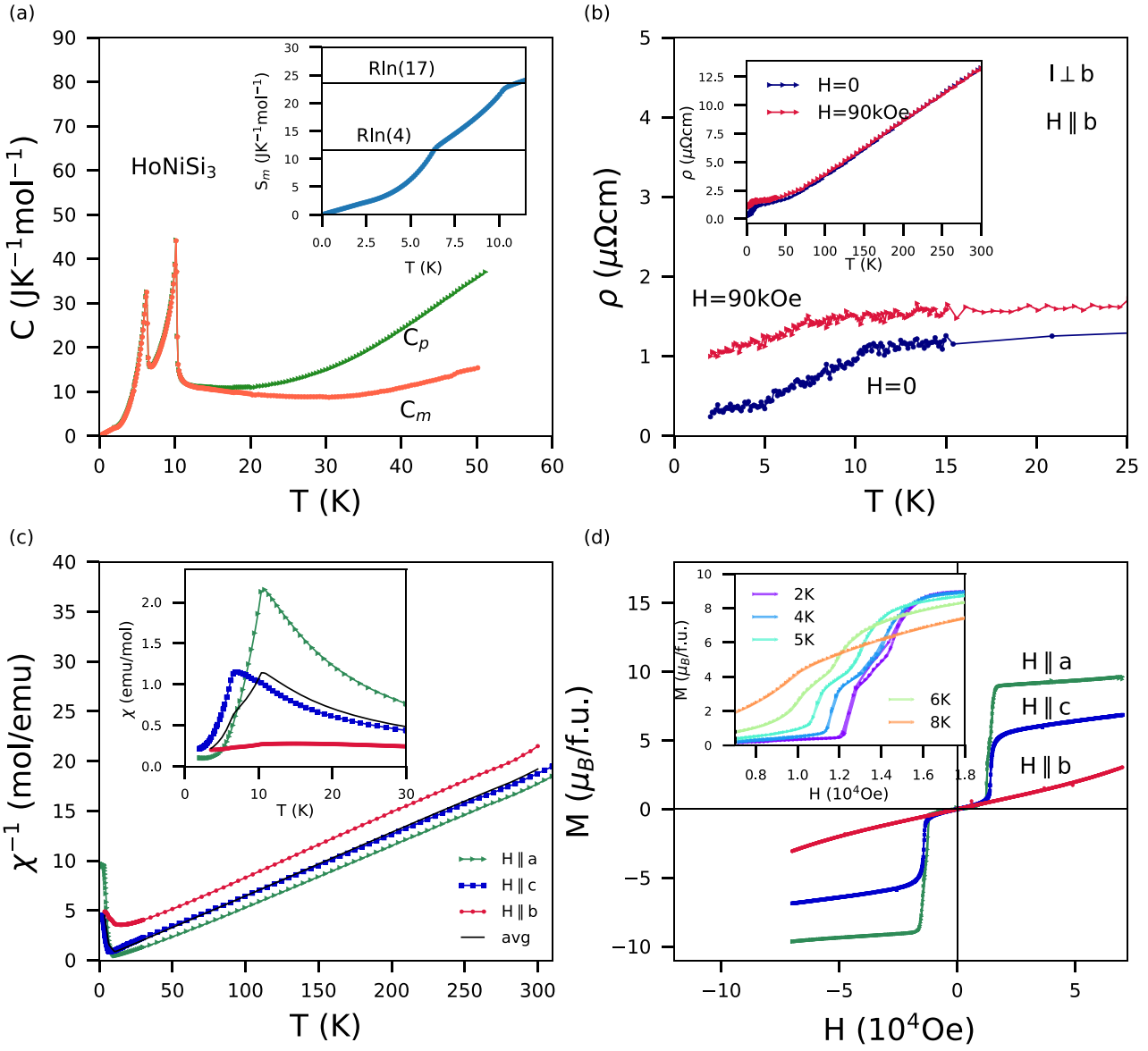

FIG. 11. Physical characterization of $HoNiSi_3$. (a) Total (C_p) and magnetic (C_m) zero-field specific heat curves. The inset portrays the released magnetic entropy. (b) Resistivity measured under zero field and 90 kOe in the temperature range where the AFM transition takes place. The inset shows the full zero-field curve up to room temperature. (c) Inverse magnetic susceptibility χ^{-1} under $H = 1000$ Oe along the **a**, **b**, and **c** axes from 2 to 300 K. The inset shows $\chi(T)$ near the magnetic transition. (d) Magnetization isotherms at 2 K in the same three directions. The inset features the isotherms near the metamagnetic transition.

contribution was not ideal in this case since C_m still shows some increase at high temperatures.

The dependence of the resistivity on T [Fig. 10(b)] shows the AFM transition with a kink around 22 K for the curves measured with and without an applied field, and the additional transition is not evident despite the high density of data points. This compound presents metallic transport behavior in the whole range of temperature, in the same way as $GdNiSi_3$ and $TbNiSi_3$.

The magnetic characterization [Figs. 10(c) and 10(d)] shows AFM ordering along the crystallographic **a** axis, albeit with different magnetic behavior between the **b** and **c** axes. The AFM transition is seen in the susceptibility measurement parallel to the axis **a** [Fig. 10(c)] as a single peak, but the polycrystalline average curve (solid black line) shows a soft plateau as a consequence of the two close transitions. The comparison between all measurements in Appendix B (Fig. 26) shows that the specific heat and the average susceptibility derivative have very similar behavior reinforcing the existence of two transitions in this compound. The fit of the Curie-Weiss law to the polycrystalline average in the high temperature limit gives $\mu_{\text{eff}} = 9.4(9)\ \mu_B$, in reasonable agreement with the theory, which predicts a value of 10.65 μ_B, but a positive paramagnetic Curie-Weiss temperature of $\theta_p = +20(2)$ K that may arise from ferromagnetic correlations in the material.

Figure 10(d) shows the dependence of the magnetization on the applied field along the three crystallographic directions. In the easy AFM **a** axis, $DyNiSi_3$ displays an initial plateau

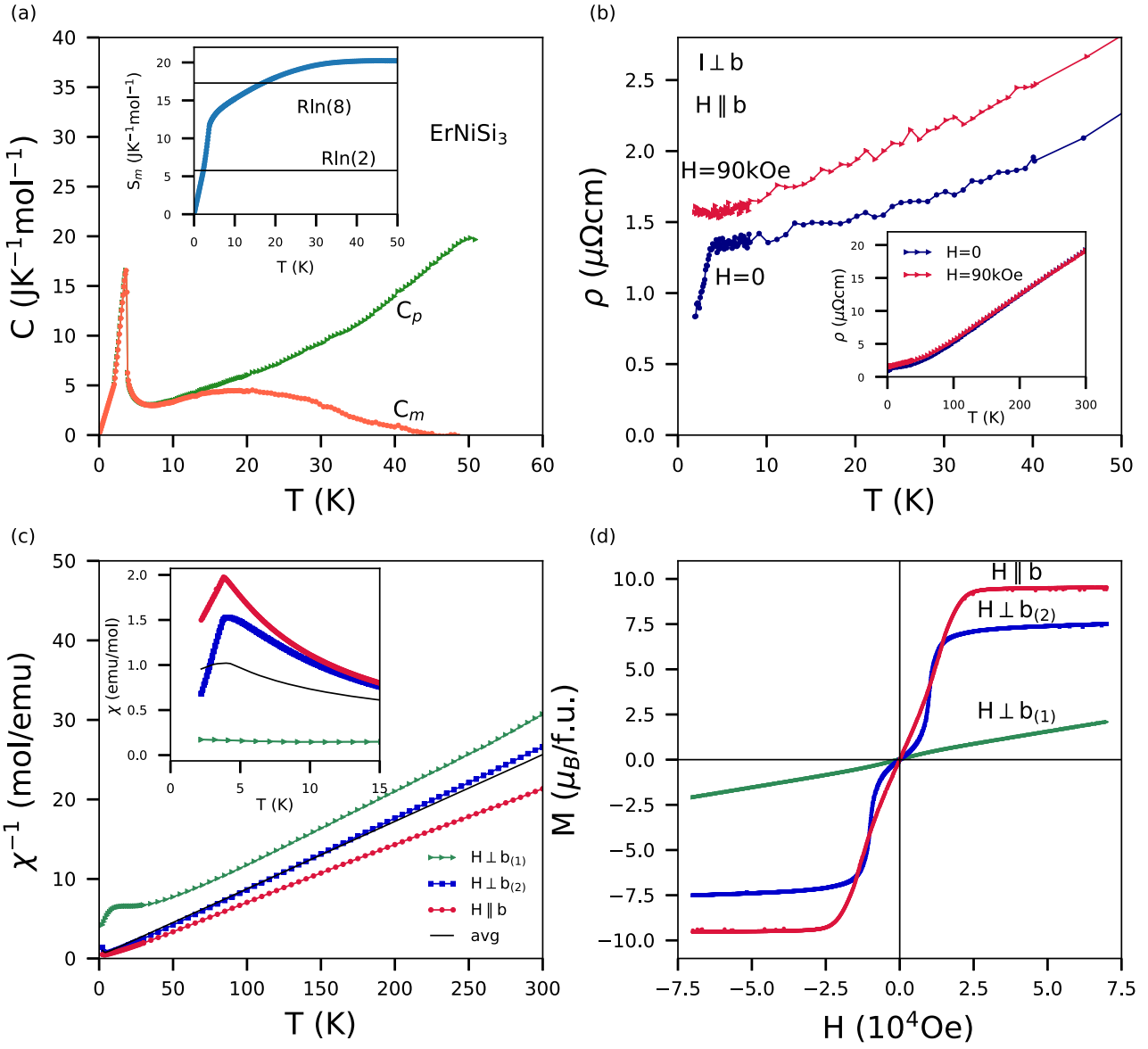

FIG. 12. Physical characterization of $ErNiSi_3$. (a) Total (C_p) and magnetic (C_m) zero-field specific heat curves. The inset portrays the released magnetic entropy. (b) Resistivity measured under zero field and 90 kOe in the temperature range where the AFM transition takes place. The inset shows the full zero-field curve up to room temperature. (c) Inverse magnetic susceptibility χ^{-1} under $H = 1000$ Oe along the **b** and the two directions perpendicular to this axis from 2 to 300 K. The inset shows $\chi(T)$ near the magnetic transition. (d) Magnetization isotherms at 2 K in the same three directions.

followed by two irreversible metamagnetic transitions, reaching saturation under an applied field of 32 kOe. The plateau inside the hysteresis achieves a magnetization of half of the saturation, indicating the reversal of a single spin in an AFM lattice with four spins.

Even though $DyNiSi_3$ presents less complex behavior than $TbNiSi_3$ [Fig. 8(d)] the shapes of the major hystereses seen in both compounds are very similar and are probably associated with the appearance of the similar magnetic structures. The main differences lie in the field intensity necessary to reorient the magnetic moments, which is higher for $TbNiSi_3$, and in the appearance of other magnetic structures at lower field values for $TbNiSi_3$. The magnetic responses along the **b** and **c** axes do not show any evidence of a metamagnetic transition but, unlike the ones for $TbNiSi_3$ and $GdNiSi_3$, they are distinct and can be associated with the presence of the two magnetic transitions observed in this compound. As shown in the next section, this is also observed for $HoNiSi_3$.

We should also mention that in our preliminary work presenting the initial results for $DyNiSi_3$ and $HoNiSi_3$ [29] the $M(H)$ curves for $DyNiSi_3$ showed the presence of multiple magnetic transitions, without reaching the saturation value, when the field was applied perpendicular to the **b** axis. Further x-ray Laue diffraction studies indicated that those measurements were taken along the (101) direction, i.e., the diagonal of the ac plane, meaning that the structures accessed during the measurements should be a competition between the ordering seen along the **a** and **c** axes.

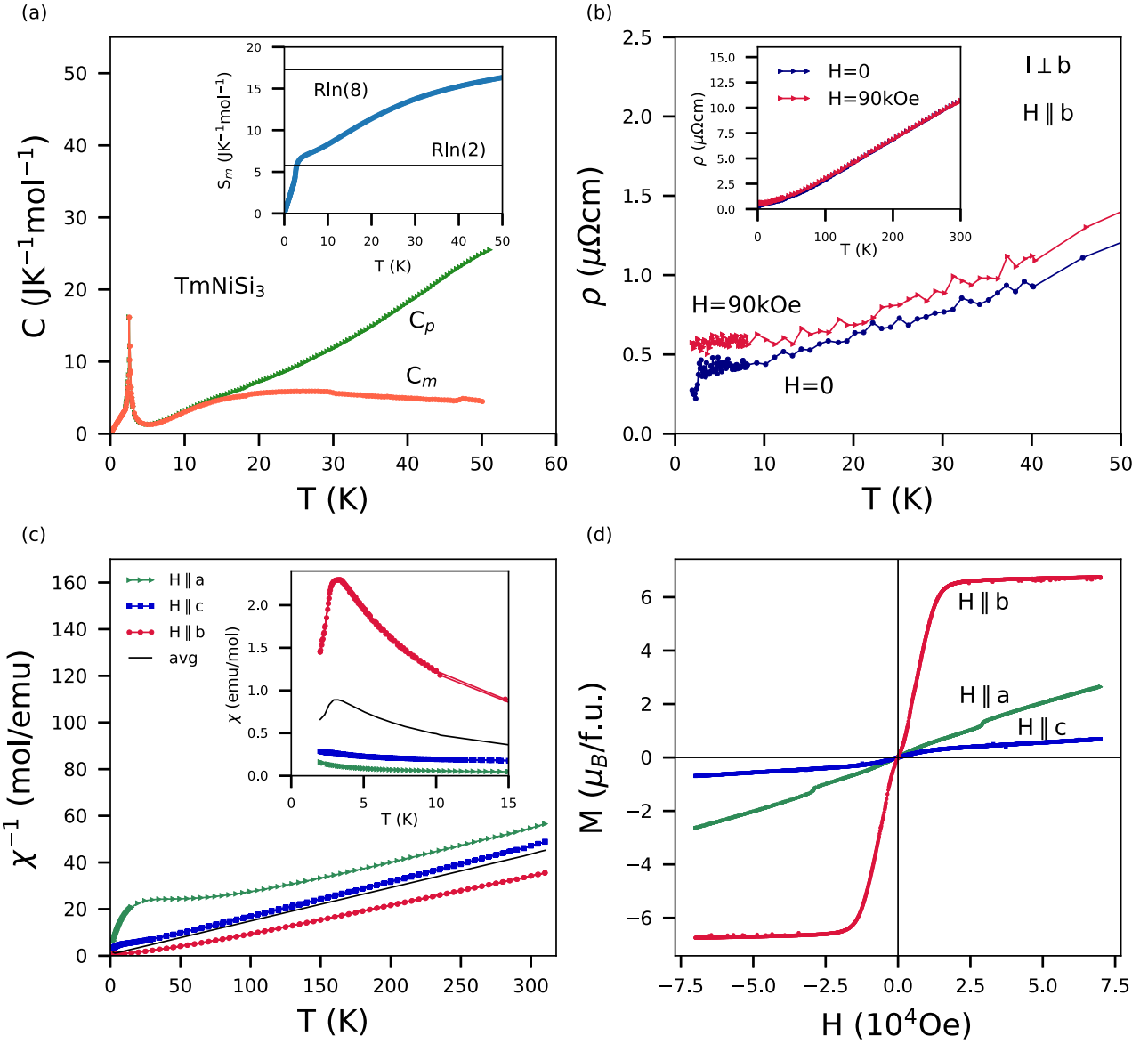

FIG. 13. Physical characterization of $TmNiSi_3$. (a) Total (C_p) and magnetic (C_m) zero-field specific heat curves. The inset portrays the released magnetic entropy. (b) Resistivity measured under zero field and 90 kOe in the temperature range where the AFM transition takes place. The inset shows the full zero-field curve up to room temperature. (c) Inverse magnetic susceptibility χ^{-1} under $H = 1000$ Oe along the **a**, **b**, and **c** axes from 2 to 300 K. The inset shows $\chi(T)$ near the magnetic transition. (d) Magnetization isotherms at 2 K in the same three directions.

E. $HoNiSi_3$

Several intermetallic compounds based on rare-earth and 3*d*-transition elements exhibit successive magnetic transitions, generally evidenced by specific heat and susceptibility measurements [2,43–45]. For the $RNiGe_3$ family, the only compound that presents such behavior is $NdNiGe_3$, with two transitions at 9.4 and 10.6 K [10]. For $HoNiSi_3$, the specific heat measurement [Fig. 11(a)] shows two sharp and distinct peaks, one at 6.3 K and the other at 10.1 K. The sharpness of the peaks indicates that this cannot be due to a Schottky anomaly, but to two distinct phase transitions. The shoulder observed in the specific heat of $DyNiSi_3$ [Fig. 10(a)] is probably associated with the same structure, but, as the temperatures are close, this is not as clear as for $HoNiSi_3$. The released magnetic entropy (inset graph) reaches $R\ln(4)$ at the first phase transition and $R\ln(17)$ at the second, a value consistent with the maximum expected value for the multiplet of the ion Ho^{3+} ($J = 8$). At higher temperatures, the nonmagnetic specific heat subtraction using $YNiSi_3$ and $LuNiSi_3$ cannot account for all lattice and electronic contribution of $HoNiSi_3$ for C_m still increases, making the evaluation above T_N less reliable.

In the resistivity [Fig. 11(b)] the high temperature transition is very apparent as in the specific heat, although the second one can only be observed in the curve measured without an applied field as a smooth kink. For the curve with $H = 90$ kOe, only one transition at ≈ 10 K is visible and the system also shows a positive magnetoresistance. As for the other compounds of this family, $HoNiSi_3$ presents metallic behavior.

The dependence of the susceptibility on the temperature [Fig. 11(c)] shows AFM ordering along both **a** and **c** axes.

TABLE III. Main parameters for the series RNiSi$_3$: T_N, θ_p, and θ_i extracted for the three crystallographic directions. The experimental effective magnetic moment (μ_{eff}) and the highest observed moment at 2 K (μ_{HF}) are also shown.

R	Easy axis	T_N (K)	θ_p (K)	θ_a (K)	θ_b (K)	θ_c (K)	μ_{eff} (μ_B)	μ_{HF} (μ_B)	χ_0 (10^{-3} emu/mol)	RRR
Y	–	–	–	–	–	–	–	–	0.08(5)	54(5)
Gd	**a**	22.2(2)	−30(3)	−36	−35	−28	8.1(2)	2.1(1)	0.40(4)	50(5)
Tb		33.2(2)	−8.0(8)	29	−96	−60	9.6(3)	9.1(2)	3.2(3)	40(4)
Dy		22.8(2), 23.6(2)	+20(2)	43	−400	−37	9.4(3)	10.8(2)	11.7(1)	64(6)
Ho		6.3(2), 10.4(3)	+1.0(1)	23	−53	8.3	11.0(3)	9.6(2)	2.0(2)	51(5)
Er	**b**	3.7(1)	−1.7(2)	−36	14	1.2(1)	9.2(3)	9.5(2)	5.3(5)	23(2)
Tm		2.6(1)	−12(1)	−24	17	−126	7.8(2)	6.7(2)	−3.1(3)	40(4)
Lu	–	–	–	–	–	–	–	–	−0.07(5)	38(4)

The susceptibility in the direction of **a** (inset) attains a higher value, but only the higher temperature transition is present. The measurement along **c** shows both transitions, although the first one has the more intense magnetic response. The difference between the curves indicates that **a** is the easy AFM axis as for the other compounds, but with a weaker ordering along the **c** axis. The magnetic moment obtained from the Curie-Weiss fit is $\mu_{\text{eff}} = 11.0(3)\ \mu_B$, close to the theoretical one of 10.61 μ_B, and the paramagnetic Curie-Weiss temperature results slightly positive and equal to $\theta_p = +1.0(1)$ K. The T_N for this compound was taken to be that of the higher temperature transition, and its average value, obtained from the curves of $C_p(T)$, $\rho(T)$, and $\partial[T\chi(T)]/\partial T$, is $T_N = 10.4(3)$ K (see Fig. 27 in Appendix B).

Figure 11(d) shows $M(H)$ measured along the three directions. The metamagnetic transitions are presented in the measurements along **a** and **c**, although the second one reaches a lower magnetization. The curve along the **a** direction displays a small hysteresis (inset) with a plateau at half of the saturation magnetization, similar to TbNiSi$_3$ and DyNiSi$_3$. The curve along **c** has a higher critical field and a single metamagnetic transition without any plateaus or hysteresis. The behavior presented by this compound suggests the presence of a component-separated magnetic transition [2], where the magnetic moment components can order independently in two distinct directions and with different critical temperatures. Nonetheless, further studies are necessary to elucidate whether this is indeed the case.

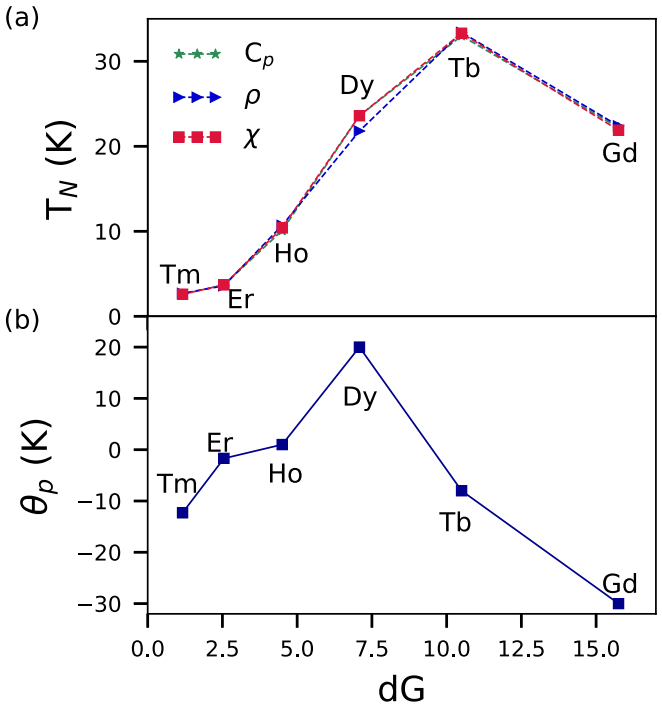

FIG. 14. (a) Dependence of the Néel temperature obtained from the experimental specific heat, resistivity, and magnetic susceptibility on the de Gennes factor $dG = (g_J - 1)^2 J(J+1)$. (b) Dependence of the paramagnetic Curie-Weiss temperature (θ_p) on dG.

F. ErNiSi$_3$

For systems containing Er^{3+}, Tm^{3+} and Yb^{3+}, we expect differences in the magnetic properties compared to those with the ions Tb^{3+}, Dy^{3+}, and Ho^{3+}, as anticipated from a change in the sign of the multiplicative factor α that appears in the Stevens' operator equivalent method [46,47]. In an intermetallic series, this manifests as a change in the direction of the ordered magnetic moments, which can go, for example, from an easy axis system for the samples with the ions Tb^{3+}, Dy^{3+}, and Ho^{3+} to a planar system for Er^{3+}, Tm^{3+}, and Yb^{3+} [11]. For the RNiGe$_3$ family, which is also orthorhombic, the AFM easy axis changes from **a** for R = Gd-Ho to **c** for R = Er, Tm [10]. For YbNiSi$_3$, the only member of the series presented in this paper that has been fully characterized, the magnetic moment of the Yb atoms are ordered along the **b** axis [25,28], in contrast with the observed for the compounds described so far here, where the AFM moments align in the **a** axis.

TABLE IV. Experimental and theoretical values of the variation of specific heat and magnetic entropy across the antiferromagnetic transition for each magnetic compound and their associated J. The values for ΔC_m and S_m are in J K^{-1} mol^{-1}.

R	J (R^{+3})	$\Delta C_m^{\text{expt}}(T_N)$	$\Delta C_m(T_N)$	$S_m^{\text{expt}}(T_N)$	$S_m(T_N)$
Gd	7/2	20	20.15	15.7	17.3
Tb	6	21	20.54	10.5	21.3
Dy	15/2	13	20.62	9.7	23.0
Ho	8	30	20.64	22.8	23.6
Er	15/2	12	20.62	12.2	23.0
Tm	6	13	20.54	6.0	21.3

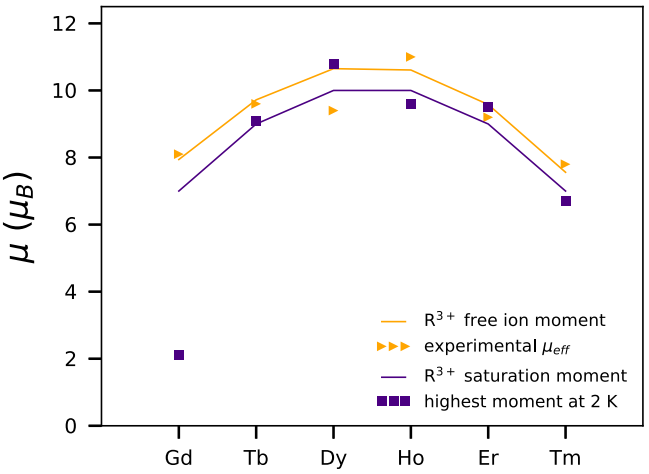

FIG. 15. Experimental effective magnetic moment and highest observed moment at 2 K. The lines indicate the theoretical value of the free rare earth ions and their saturation moment.

$ErNiSi_3$ has $T_N = 3.7(1)$ K (see Fig. 28 in Appendix B) that appears as a sharp discontinuity on the high-temperature side of the transition in the specific heat in Fig. 12(a). The released magnetic entropy still increases above T_N and then attains a constant value above $R\ln(8)$.

The resistivity [Fig. 12(b)] shows metallic behavior with an anomaly at T_N. A positive magnetoresistance appears at low temperatures.

The determination of the axes **a** and **c** by the Laue diffraction was not possible in this case due to the parasitic phase in the crystals, so we have labeled those two directions as $\perp\mathbf{b}_{(1)}$ and $\perp\mathbf{b}_{(2)}$ in Fig. 12(c). The curves measured parallel to **b** and in one of the perpendicular directions have similar behavior indicating that, as with $HoNiSi_3$, $ErNiSi_3$ also must have a second AFM axis, despite the lack of a second transition in the specific heat. The fit of the Curie-Weiss law yields $\mu_{\text{eff}} = 9.2(3)\ \mu_B$, in agreement with the theoretical value of 9.58 μ_B, and $\theta_p = -1.7(2)$ K, that reflects the AFM ordering of this material.

Figure 12(d) shows the magnetization versus field curves at 2 K, where the curve for $H \parallel \mathbf{b}$ reaches saturation with paramagneticlike behavior. One of the curves for $H \perp \mathbf{b}$ shows a smooth metamagnetic transition, but does not saturate, while the other one shows a small magnetization along the field. The results seen in Figs. 12(c) and 12(d) indicate an easy axis along **b**, although there is also an ordering seen along the direction $\perp\mathbf{b}_{(2)}$. The low T_N of this compound probably smooths the transitions of the $M(H)$ isotherms at 2 K when compared to the previous samples, which may explain the lack of a plateau in those curves.

G. $TmNiSi_3$

The last compound studied in this work, $TmNiSi_3$, shows the lowest Néel temperature among them, with $T_N = 2.6(1)$ K (see Fig. 29). Figure 13 shows the physical characterization performed for this material. The specific heat [Fig. 13(a)] shows a sharp peak at low temperature, with the released magnetic entropy reaching a value of $R\ln(2)$ at T_N. The broad

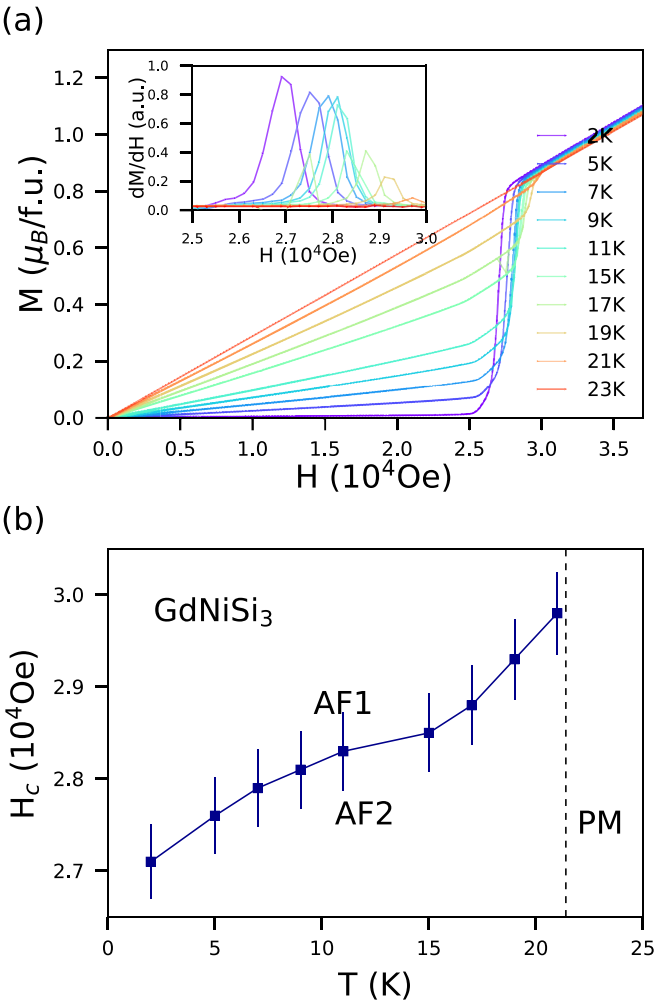

FIG. 16. (a) Magnetic field dependence of magnetization for $GdNiSi_3$, taken at several temperatures indicated in the figure. The inset shows the derivative dM/dH curves. (b) Temperature dependence of the critical field.

curvature above 10 K is probably due to a Schottky anomaly resulting from the splitting of the ground state by the crystal electric field, a phenomenon commonly observed in other rare earth-based intermetallic systems [48–51]. The temperature dependence of the resistivity [Fig. 13(b)] shows the magnetic transition in the curve with no applied field, while under a field of $H = 90$ kOe this transition is not visible. Similarly to the other compounds, the resistivity follows metallic behavior and a positive magnetoresistance.

The magnetic characterization [Figs. 13(c) and 13(d)] shows an easy AFM axis along **b** but, contrary to $ErNiSi_3$, the magnetic anomaly along the **a** axis is weaker. The fit of the Curie-Weiss law to the susceptibility curve [Fig. 13(c)] leads to an effective moment of $\mu_{\text{eff}} = 7.8(2)\ \mu_B$, in good agreement with the theoretical prediction of 7.56 μ_B, and $\theta_p = -12(1)$ K. Figure 13(d) shows the dependence of the magnetization on the applied field, with a paramagneticlike response parallel to **c**, and a saturation along **b**. The curve parallel to **a** shows a small step around 28 kOe, but saturation is only achieved with applied field parallel to **b**.

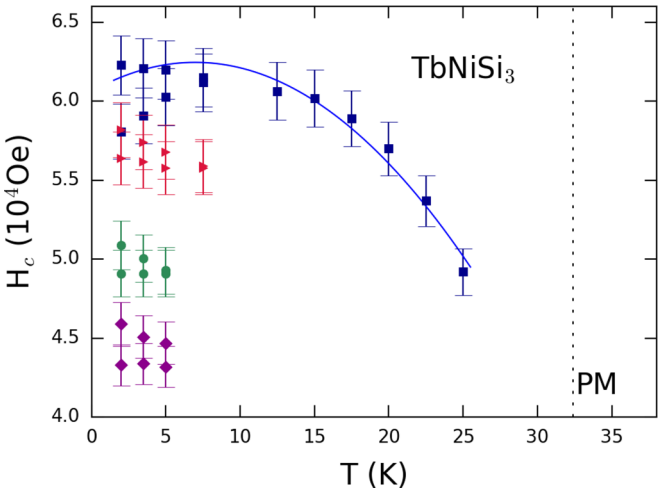

FIG. 17. Magnetic phase diagram for $TbNiSi_3$. The dashed line indicates T_N and delimits the paramagnetic phase (PM).

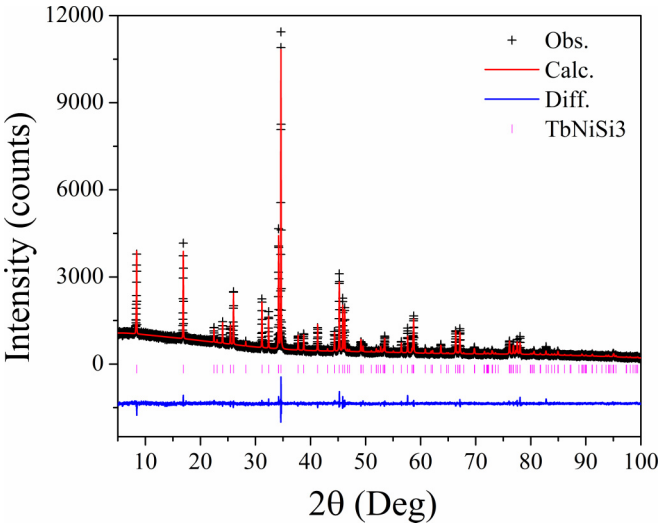

FIG. 19. Rietveld plot for $TbNiSi_3$. The black crosses represent observed data, the red line indicates the calculated pattern, and the blue line at the bottom represents the difference between the observed and calculated patterns. The vertical bars indicate Bragg reflections of each identified phase.

V. DISCUSSION

The compounds of the $RNiSi_3$ series (R = Y, Gd-Tm, Lu) display rich physical behavior, notably in their magnetic properties, with some features common to all such as anisotropic magnetizations, AFM ground states, and the presence of metamagnetic transitions for R = Gd-Tm. There are, nonetheless, idiosyncrasies that set each one apart. Table III summarizes the main properties found for the single crystals of this series.

In systems where the magnetism originates solely from the rare earth ions, it is frequent that the magnetic ordering temperature is scaled by the de Gennes factor $dG = (g_J - 1)^2 J(J+1)$, with the Gd-based compound ($g_J = 2$ and $J = 7/2$) displaying the highest temperature. This is a consequence of the long range nature of the interactions between the magnetic moments, well described by the RKKY model, which states that the effective exchange constant ($\mathcal{J}$) is proportional to dG, and $\mathcal{J}$ is often proportional to the critical temperature. There are systems, however, where this scaling is not observed, such as the series $RNiGe_3$ [10], RCu_2 [52], and RMg_2Cu_9 [45], due to crystal electric field effects and exchange anisotropy. These factors change the system Hamiltonian and, therefore, lead to deviations from the proportionality expected from the case where only RKKY is taken into account. Usually the models including those extra terms predict an increase in the ordering temperature when CEF is important; however

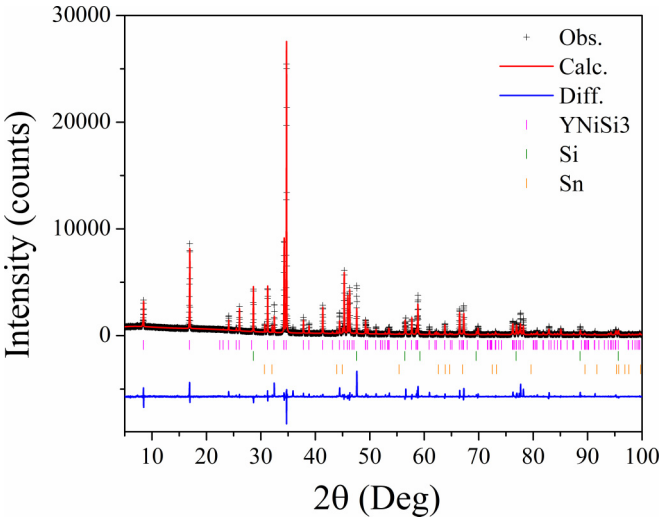

FIG. 18. Rietveld plot for $YNiSi_3$. The black crosses represent observed data, the red line indicates the calculated pattern, and the blue line at the bottom represents the difference between the observed and calculated patterns. The vertical bars indicate Bragg reflections of each identified phase.

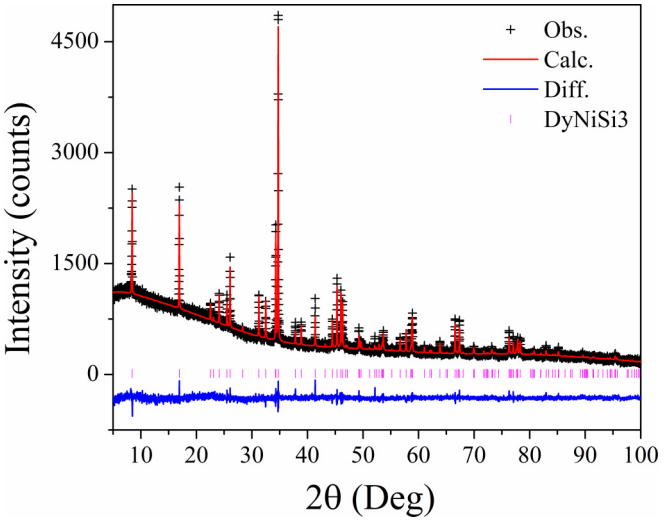

FIG. 20. Rietveld plot for $DyNiSi_3$. The black crosses represent observed data, the red line indicates the calculated pattern, and the blue line at the bottom represents the difference between the observed and calculated patterns. The vertical bars indicate Bragg reflections of each identified phase.

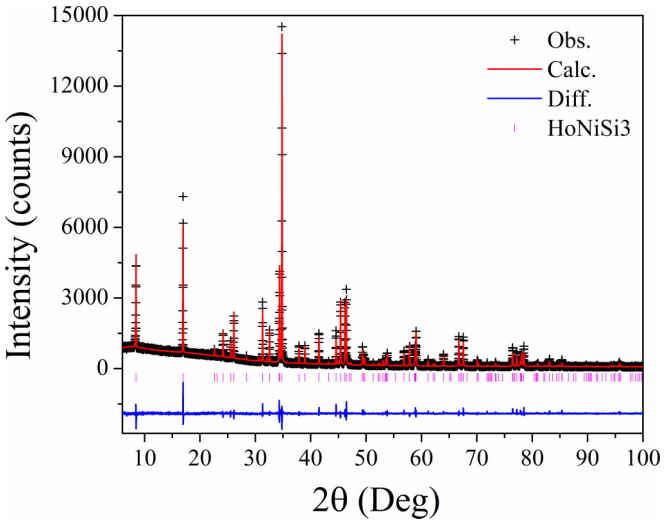

FIG. 21. Rietveld plot for $HoNiSi_3$. The black crosses represent observed data, the red line indicates the calculated pattern, and the blue line at the bottom represents the difference between the observed and calculated patterns. The vertical bars indicate Bragg reflections of each identified phase.

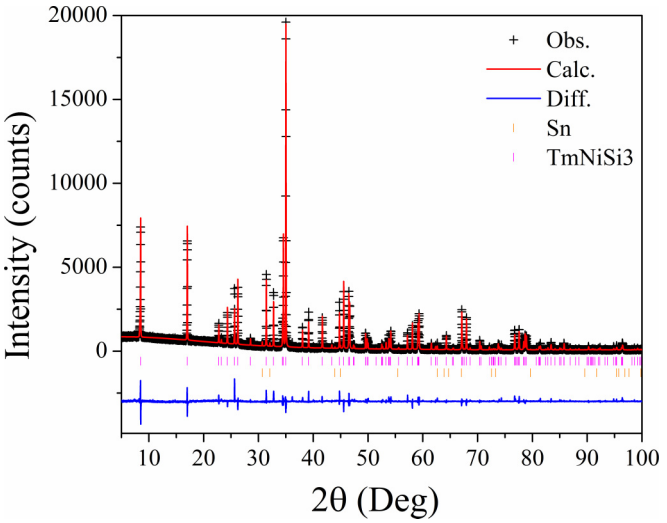

FIG. 23. Rietveld plot for $TmNiSi_3$. The black crosses represent observed data, the red line indicates the calculated pattern, and the blue line at the bottom represents the difference between the observed and calculated patterns. The vertical bars indicate Bragg reflections of each identified phase.

the competition between two stable ordered phases can lower this temperature [53].

Figure 14(a) shows the dependence of T_N on dG obtained from C_p, ρ, and χ, with an excellent agreement between the different techniques, which strongly deviates from the expected trend. From the complex magnetic behavior presented by those compounds in the previous sections, crystal field effects must have a profound effect on their properties, so deviation from linear scaling with de Gennes factor is not surprising.

Magnetic transitions are seen very clearly in the specific heat measurements, allowing us to confirm two transitions in $DyNiSi_3$ and $HoNiSi_3$, which are less sharp in magnetic and resistivity data. In the compounds with a single transition, its specific heat takes a lambda shape around the critical point, associated with a second-order phase transition [54]. Table IV presents the experimental variation of specific heat $[\Delta C_m^{\text{expt}}(T_N)]$ and magnetic entropy $[S_m^{\text{expt}}(T_N)]$ across the

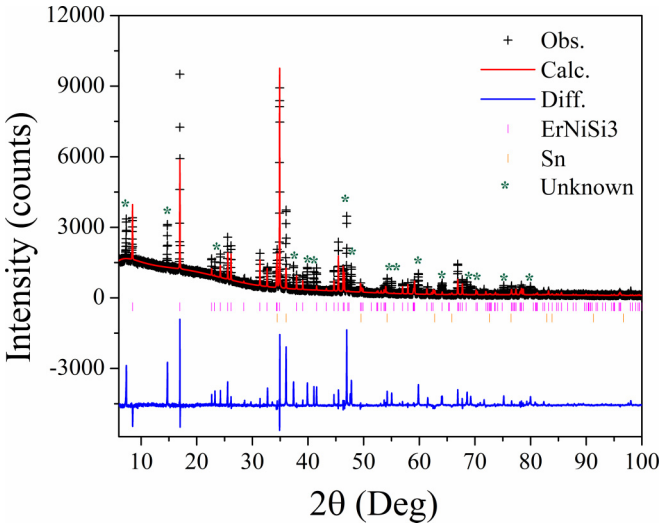

FIG. 22. Rietveld plot for $ErNiSi_3$. The black crosses represent observed data, the red line indicates the calculated pattern, and the blue line at the bottom represents the difference between the observed and calculated patterns. The vertical bars indicate Bragg reflections of each identified phase. The Bragg reflections highlighted with asterisks stand for some unidentified impurity (-ies) that is (are) growing simultaneously with the $ErNiSi_3$ crystal.

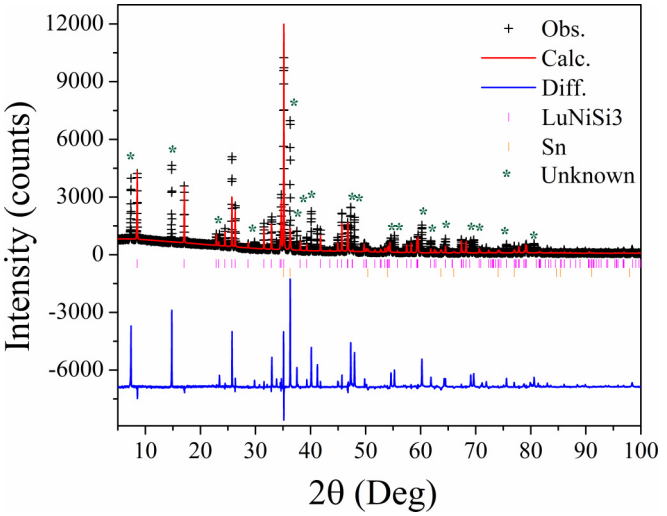

FIG. 24. Rietveld plot for $LuNiSi_3$. The black crosses represent observed data, the red line indicates the calculated pattern, and the blue line at the bottom represents the difference between the observed and calculated patterns. The vertical bars indicate Bragg reflections of each identified phase. The green asterisks represent an (some) unknown phase(s) that is (are) growing together with the $LuNiSi_3$ crystal.

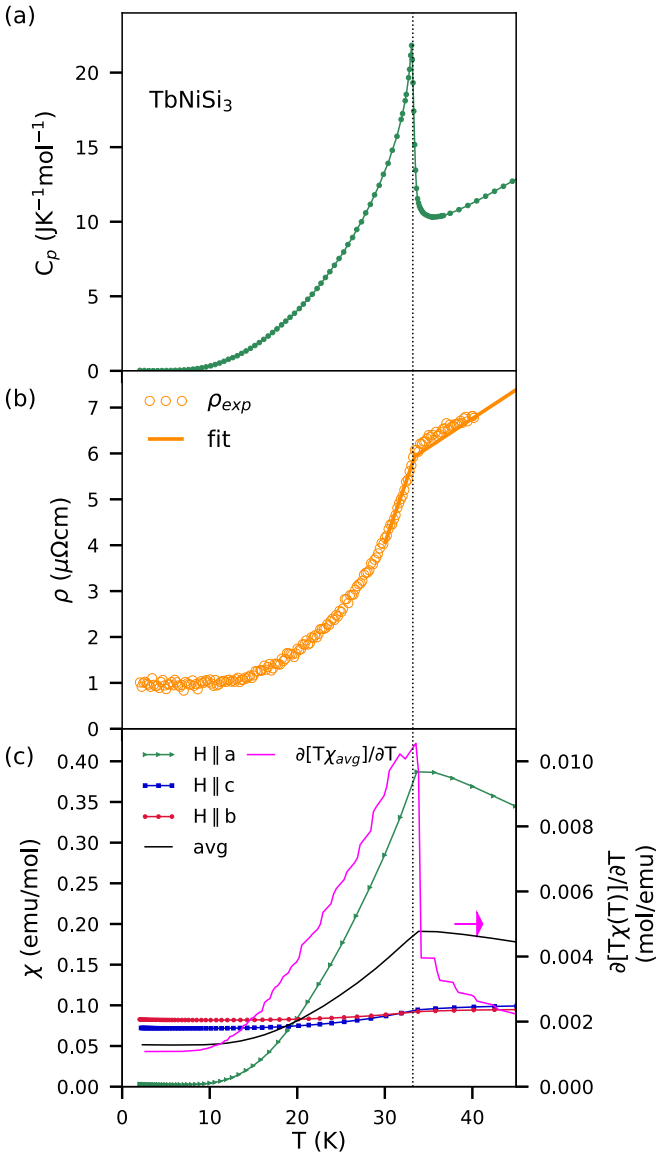

FIG. 25. Determination of the Néel temperature for $TbNiSi_3$ from (a) specific heat, (b) resistivity, and (c) magnetic susceptibility measurements. The dashed line indicates the average Néel temperature obtained from the three measurements.

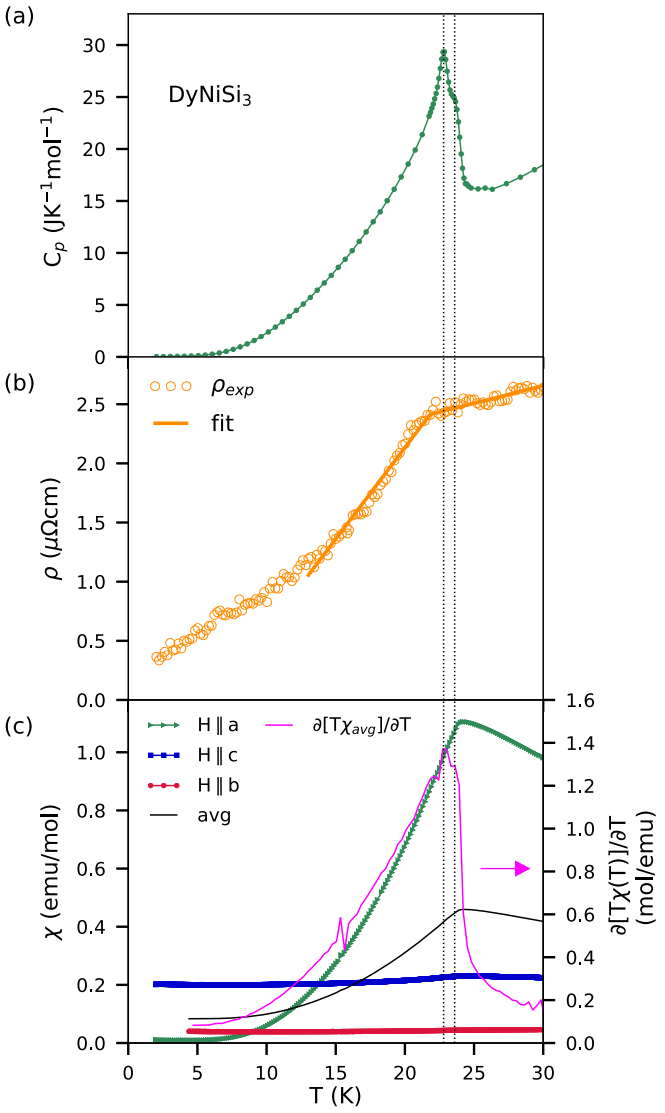

FIG. 26. Determination of the Néel temperature for $DyNiSi_3$ from (a) specific heat, (b) resistivity, and (c) magnetic susceptibility measurements. The dashed lines indicate the average transition temperatures obtained from the specific heat and susceptibility measurements.

transition, as well as $\Delta C_m(T_N) = 5RJ(J+1)/[(J+1)^2 + J^2]$, predicted by mean field theory [55], and the maximum magnetic entropy $S_m^{\max} = R\ln(2J+1)$, calculated without taking into account the splitting of the energy levels due to CEF effects. $GdNiSi_3$ has a value of $\Delta C_m^{\text{expt}}(T_N)$ equivalent to the one predicted by theory; however $HoNiSi_3$ has a much higher $\Delta C_m^{\text{expt}}(T_N)$, while $S_m^{\text{expt}}(T_N)$ attains its full value, indicating a first order transition. For the remaining compounds, ΔC_m^{exp} does not exceed the theoretical value, and observed magnetic entropy stays well below the theoretical value, due to CEF splitting the ground state.

Compared to $GdNiGe_3$ ($T_N = 26.2$ K) [18], $GdNiSi_3$ has a lower $T_N = 22.2$ K despite the smaller lattice parameters. This is also observed for $TbNiGe_3$ ($T_N = 35.6$ K) and $ErNiGe_3$ ($T_N = 5.8$ K) that also have higher ordering temperatures than $TbNiSi_3$ ($T_N = 33.2$ K) and $ErNiSi_3$ ($T_N = 3.7$ K), respectively. The competition between two different magnetic phases that leads to two phase transitions for $DyNiSi_3$ and $HoNiSi_3$, must play a role in those lower ordering temperatures observed in this series, despite their smaller unit cells.

The lower T_N of $GdNiSi_3$ than $TbNiSi_3$ and $DyNiSi_3$ must be a consequence of the lack of CEF effects in the Gd compound. It is also important to point out that the appearance of the hysteresis in $TbNiSi_3$, $DyNiSi_3$, and $HoNiSi_3$ is probably associated with a higher effective exchange constant that can affect the ordering temperatures. The θ_p [Fig. 14(b)] reflects the high magnetic anisotropy of those compounds, with $DyNiSi_3$ and $HoNiSi_3$ exhibiting positive values that can be associated with ferromagnetic interactions present in those samples. The Gd-based compound displays the highest absolute value.

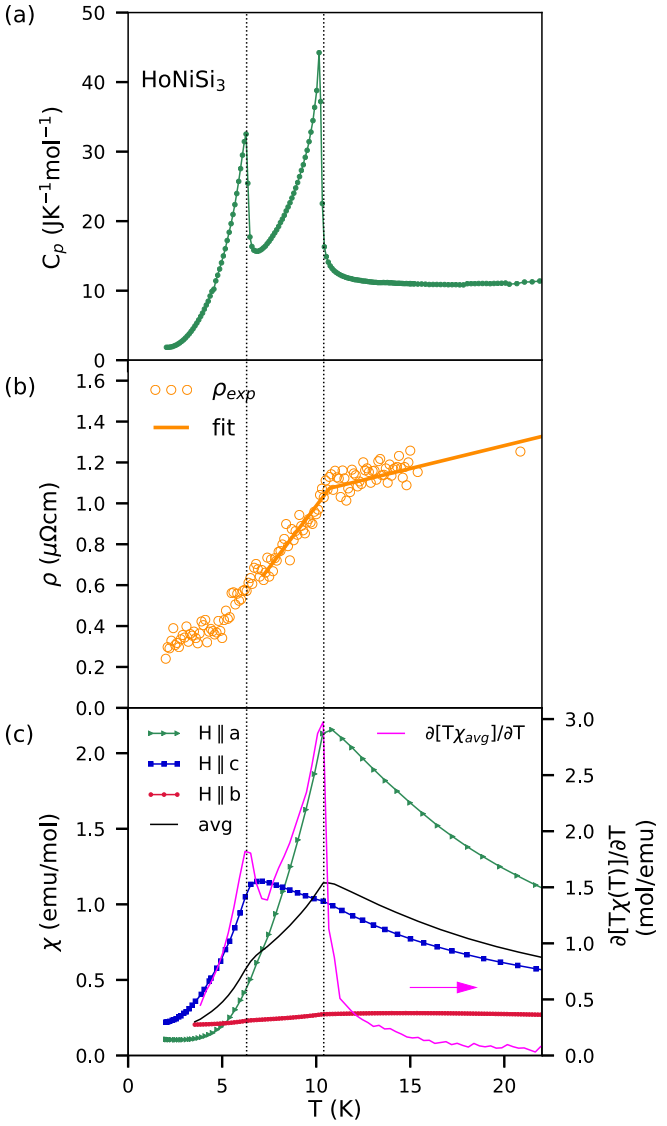

FIG. 27. Determination of the Néel temperature for $HoNiSi_3$ from (a) specific heat, (b) resistivity, and (c) magnetic susceptibility measurements. The dashed lines indicate the average transition temperatures obtained from the specific heat and susceptibility measurements for the transition at 6.3 K, and from the three measurements at 10.4 K.

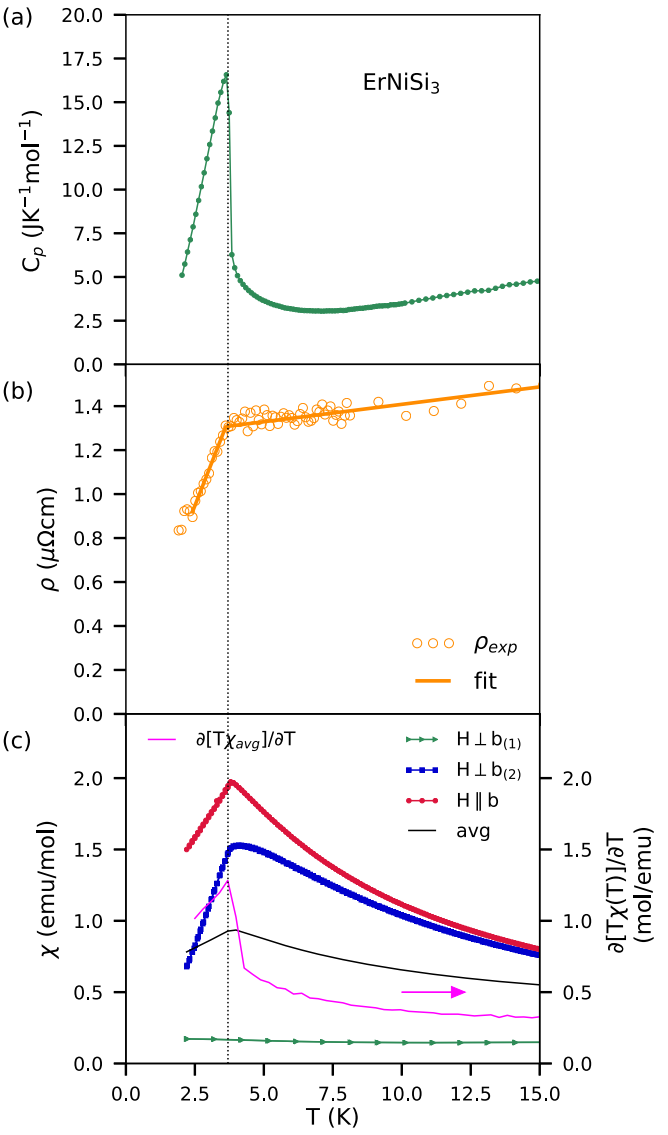

FIG. 28. Determination of the Néel temperature for $ErNiSi_3$ from (a) specific heat, (b) resistivity, and (c) magnetic susceptibility measurements. The dashed line indicates the average Néel temperature obtained from the three measurements.

Figure 15 shows the dependence of μ_{eff} observed for the rare earth of each compound, as well as the highest observed magnetic moment at 2 K of the magnetization versus applied field curves. The lines display the theoretical magnetic moment of the free trivalent rare earth ion and their saturation moment. The values obtained for μ_{eff} are in excellent agreement with the expected value of the rare earth ions, indicating that the magnetism of those compounds originates solely from those ions, while the Ni atoms are nonmagnetic.

$GdNiSi_3$ is the only member of the series in which magnetization does not saturate at 2 K with an applied field of 70 kOe. The magnetization after the metamagnetic transition corresponds to only about 0.82 μ_B [Fig. 7(d)], about 1/8 of the expected saturation value of the ion Gd^{3+} (7.0 μ_B). The same transition is observed for $GdNiGe_3$ [10], with similar critical fields and magnetic moment values, indicating that the magnetic structure of both compounds are similar. Figure 16(a) shows this transition along a range of temperatures, as well as the derivative curves in the inset that were used to estimate their critical fields H_c. It is noteworthy that the linear extrapolation of the $M(H)$ data above H_c to $H = 0$ goes to the origin. This fact indicates that the transition at H_c is not a spin flip transition as observed in other rare-earth compounds, but a spin flop transition in the antiferromagnetic state [56]. As the temperature increases, the transition becomes less pronounced while the critical field increases [Fig. 16(b)]. The latter is unusual for most compounds that undergo a magnetic transition, although some paramagnetic systems show the same effect in the field-induced transition to the FM state [57,58]. More interestingly, Gd_5Ge_4 displays a metamagnetic transition along its AFM axis [59,60] with very similar behavior to $GdNiSi_3$ and $GdNiGe_3$. Moreover, it can also undergo a transition to a FM state, depending on the direction and intensity of the

applied field, which suggests that $GdNiSi_3$ is a good candidate for studies using high magnetic fields.

In addition, among the $RNiSi_3$ series, $GdNiSi_3$ presents the magnetic response most similar to the corresponding compound of the series $RNiGe_3$. Despite T_N of the two series being comparable, the series $RNiSi_3$ has more complex magnetic behavior, with the presence of multiple magnetic transitions and hysteresis that are not observed in the $RNiGe_3$ series. Since the Gd-based compounds of the series resemble each other, the change in the crystal electric field due to the substitution of Ge by Si should play a key role to understand those differences between the series.

The oscillatory and long-range nature of the RKKY interaction, which can favor either FM or AFM ordering, often induces the appearance of magnetic structures that can be commensurate or incommensurate with the crystal lattice [61,62]. A compound may show several intermediate magnetic phases, which can be accessed changing the temperature or the magnetic field, generating complex magnetic phase diagrams [63,64] such as that for $TbNiSi_3$. Figure 17 shows a tentative phase diagram for this system using the critical fields of the magnetization curves shown in Fig. 8(d). There are at least four distinct magnetically ordered states, in addition to the hysteresis that suggest the presence of a FM component.

$HoNiSi_3$ offers an additional challenge due to its two magnetic phase transitions that manifest in different directions. As discussed previously, this can result from an independent ordering of the magnetic moment components along the two axes. The complex magnetic structure of this and the other compounds, however, can only be fully understood by resolving the magnetic structures responsible for our macroscopic observations, using a microscopic technique. For $ErNiSi_3$ and $TmNiSi_3$, the low magnetic ordering temperature leads to smooth transitions at 2 K, and thus require measurements at lower temperatures to properly check for metamagnetic transitions.

VI. SUMMARY

We have presented here comprehensive work on characterizing the ground states and low temperature behaviors of the intermetallic $RNiSi_3$ series (R = Y, Gd-Tm), which crystallizes in the orthorhombic space group $Cmmm$. For R = Gd-Tm, the compounds have anisotropic AFM ground states with T_N between 2.6 ($TmNiSi_3$) up to 33.2 K ($TbNiSi_3$). $YNiSi_3$ and $LuNiSi_3$ do not present antiferromagnetic ordering, but have an anisotropic susceptibility. The dependence of the magnetization on the applied field shows complex behavior, with all antiferromagnetic compounds presenting metamagnetic transitions and in some cases hysteretic behavior ($TbNiSi_3$, $DyNiSi_3$, and $HoNiSi_3$). The features exhibited by these compounds, especially $TbNiSi_3$, $DyNiSi_3$, and $HoNiSi_3$, make them good candidates for future neutron diffraction studies to resolve their magnetic structures and elucidate the observed behaviors.

ACKNOWLEDGMENTS

The authors acknowledge financial support from Brazilian funding agencies CAPES, CNPq (Contract No. 168255/2014-6), FAPESP (Contracts No. 2011/19924-2, No. 2012/17562-9, and No. 2014/20365-6) and Colombian agency COLCIENCIAS (Convocatoria doctorados nacionales No. 757 de 2016). The authors gratefully thank C. Rettori, P. C. Canfield, and S. L. Bud'ko for enlightening discussions, R. M. Coutinho for the English revision, and Eduardo M. Bittar for allowing access to the PPMS DynaCool from Quantum Design at CBPF/Rio de Janeiro, as well as two anonymous referees for valuable comments. The authors are grateful to the Multiuser Central Facilities (UFABC) for the experimental support.

APPENDIX A: RIETVELD PLOT FOR THE $RNiSi_3$ SERIES

Figures 18–24 show the Rietveld refinements for all compounds of the $RNiSi_3$ series, except for $GdNiSi_3$ that was shown in Fig. 2.

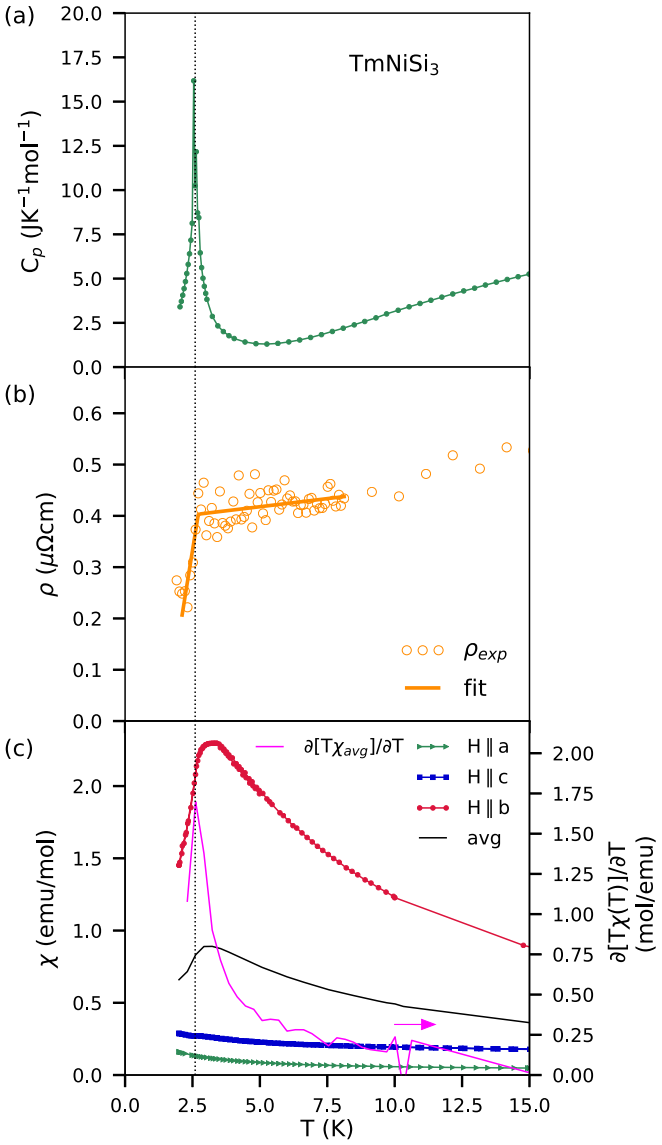

FIG. 29. Determination of the Néel temperature for $TmNiSi_3$ from (a) specific heat, (b) $d\rho/dT$, and (c) $d\chi/dT$. The dashed line indicates the average Néel temperature obtained from the three measurements.

APPENDIX B: EVALUATION OF THE TRANSITIONS TEMPERATURES

Magnetic transition temperatures can be evaluated accessing different physical properties, as specific heat, resistivity, and susceptibility. Following the discussion presented above, we show here the determination of the transition temperatures of each compound, beginning with $TbNiSi_3$ in Fig. 25.

$TbNiSi_3$ shows a single transition clearly presented in all measurements. $DyNiSi_3$ (Fig. 26), on the other hand, shows two close phase transitions that could not be completely resolved even with smaller temperature steps in the measurements. In its resistivity curve [Fig. 26(b)] the transitions seem to happen at lower temperatures than in $C_p(T)$ and $\chi(T)$, but as there is some instrumental noise we chose to only use the specific heat and magnetization measurements to evaluate T_N.

Figure 27 shows the characterization for $HoNiSi_3$. In this case the two transitions are very clear in $C_p(T)$ and $\partial[T\chi(T)]/\partial T$, but in resistivity only the high temperature transition is evident.

Figures 28 and 29 show the determination of T_N for $ErNiSi_3$ and $TmNiSi_3$, respectively.

[1] Z. Islam, C. Detlefs, A. I. Goldman, S. L. Bud'ko, P. C. Canfield, J. P. Hill, D. Gibbs, T. Vogt, and A. Zheludev, Phys. Rev. B **58**, 8522 (1998).

[2] T. Shigeoka, T. Fujiwara, K. Munakata, K. Matsubayashi, and Y. Uwatoko, J. Phys.: Conf. Ser. **273**, 012127 (2011).

[3] V. N. Nikiforov, M. Baran, A. Jedrzejczak, and V. Y. Irkhin, Eur. Phys. J. B **86**, 238 (2013).

[4] S. Jang, B. White, P. Ho, N. Kanchanavatee, M. Janoschek, J. Hamlin, and M. Maple, J. Phys.: Condens. Matter **26**, 425601 (2014).

[5] F. Kneidinger, H. Michor, E. Bauer, A. Gribanov, A. Lipatov, Y. Seropegin, J. Sereni, and P. Rogl, Phys. Rev. B **88**, 024423 (2013).

[6] E. Schuberth, M. Tippmann, L. Steinke, S. Lausberg, A. Steppke, M. Brando, C. Krellner, C. Geibel, R. Yu, Q. Si *et al.*, Science **351**, 485 (2016).

[7] J. Chen, K. Semeniuk, Z. Feng, P. Reiss, P. Brown, Y. Zou, P. W. Logg, G. I. Lampronti, and F. M. Grosche, Phys. Rev. Lett. **116**, 127001 (2016).

[8] C. Ritter, S. Kilcoyne, and R. Cywinski, J. Phys.: Condens. Matter **3**, 727 (1991).

[9] S. Kennedy, J. Wang, S. Campbell, M. Hofmann, and S. Dou, J. Appl. Phys. **115**, 172617 (2014).

[10] E. D. Mun, S. L. Bud'ko, H. Ko, G. J. Miller, and P. C. Canfield, J. Magn. Magn. Mater. **322**, 3527 (2010).

[11] M. A. Avila, S. L. Bud'ko, and P. C. Canfield, J. Magn. Magn. Mater. **270**, 51 (2004).

[12] J. Ferstl, H. Rosner, and C. Geibel, Physica B: Condens. Matter **378**, 744 (2006).

[13] T. Fujiwara, N. Aso, H. Yamamoto, M. Hedo, Y. Saiga, M. Nishi, Y. Uwatoko, and K. Hirota, J. Phys. Soc. Jpn. **76**, 60 (2007).

[14] S. Ran, S. L. Bud'ko, and P. C. Canfield, Philos. Mag. **91**, 4388 (2011).

[15] R. Lemaire, D. Paccard, R. Pauthenet, and J. Schweizer, J. Appl. Phys. **39**, 1092 (1968).

[16] K. Taylor, Adv. Phys. **20**, 551 (1971).

[17] R. J. Goetsch, V. K. Anand, and D. C. Johnston, Phys. Rev. B **87**, 064406 (2013).

[18] E. D. Mun, S. L. Bud'ko, A. Kreyssig, and P. C. Canfield, Phys. Rev. B **82**, 054424 (2010).

[19] M. Nakashima, K. Tabata, A. Thamizhavel, T. C. Kobayashi, M. Hedo, Y. Uwatoko, K. Shimizu, R. Settai, and Y. Ōnuki, J. Phys.: Condens. Matter **16**, L255 (2004).

[20] H. Sato, H. Yamaoka, Y. Utsumi, H. Nagata, M. A. Avila, R. A. Ribeiro, K. Umeo, T. Takabatake, Y. Zekko, J. Mizuki *et al.*, Phys. Rev. B **89**, 045112 (2014).

[21] K. Umeo, N. Hosogi, M. A. Avila, and T. Takabatake, Phys. Status Solidi B **247**, 751 (2010).

[22] J. K. Gorelenko, O. I. Bodak, E. I. Gladyshevskii, and V. I. Yarovets, Ukrainskii Fizichnii Zhurnal **22**, 1020 (1977).

[23] X. Chen, P. Larson, S. Sportouch, P. Brazis, S. Mahanti, C. Kannewurf, and M. Kanatzidis, Chem. Mater. **11**, 75 (1999).

[24] J. Kończyk, P. Demchenko, G. Demchenko, O. Bodak, and B. Marciniak, Acta Crystallogr. Sect. E **61**, 259 (2005).

[25] M. A. Avila, M. Sera, and T. Takabatake, Phys. Rev. B **70**, 100409 (2004).

[26] S. L. Bud'ko, P. C. Canfield, M. A. Avila, and T. Takabatake, Phys. Rev. B **75**, 094433 (2007).

[27] K. Grube, T. Wolf, P. Adelmann, C. Meingast, and H. v. Löhneysen, Physica B: Condens. Matter **378**, 750 (2006).

[28] Y. Kobayashi, T. Onimaru, M. A. Avila, K. Sasai, M. Soda, K. Hirota, and T. Takabatake, J. Phys. Soc. Jpn. **77**, 124701 (2008).

[29] D. Aristiźabal-Giraldo, F. R. Arantes, F. N. Costa, F. F. Ferreira, R. A. Ribeiro, and M. A. Avila, Phys. Proc. **75**, 545 (2015).

[30] M. E. Fisher, Philos. Mag. **7**, 1731 (1962).

[31] M. Escorne, A. Mauger, D. Ravot, and J. Achard, J. Phys. C **14**, 1821 (1981).

[32] S. Alexander, J. Helman, and I. Balberg, Phys. Rev. B **13**, 304 (1976).

[33] V. M. R. Muggeo, Stat. Med. **22**, 3055 (2003).

[34] V. M. R. Muggeo, R News **8**(1), 20 (2008).

[35] J. I. Facio, D. Betancourth, N. C. Bolecek, G. Jorge, P. Pedrazzini, V. Correa, P. S. Cornaglia, V. Vildosola, and D. García, J. Magn. Magn. Mater. **407**, 406 (2016).

[36] M. Bouvier, P. Lethuillier, and D. Schmitt, Phys. Rev. B **43**, 13137 (1991).

[37] M. Rotter, M. Loewenhaupt, M. Doerr, A. Lindbaum, H. Sassik, K. Ziebeck, and B. Beuneu, Phys. Rev. B **68**, 144418 (2003).

[38] F. Simon, A. Rockenbauer, T. Fehér, A. Jánossy, C. Chen, A. J. S. Chowdhury, and J. W. Hodby, Phys. Rev. B **59**, 12072 (1999).

[39] H. Yamada and S. Takada, J. Phys. Soc. Jpn. **34**, 51 (1973).

[40] J. Jensen and A. R. Mackintosh, *Rare Earth Magnetism* (Clarendon, Oxford, 1991).

[41] G. Drachuck, A. E. Böhmer, S. L. Bud'ko, and P. C. Canfield, J. Magn. Magn. Mater. **417**, 420 (2016).

[42] T. Shigeoka, H. Fujii, M. Nishi, Y. Uwatoko, T. Takabatake, I. Oguro, K. Motoya, N. Iwata, and Y. Ito, J. Phys. Soc. Jpn. **61**, 4559 (1992).
[43] R. Watanuki, G. Sato, K. Suzuki, M. Ishihara, T. Yanagisawa, Y. Nemoto, and T. Goto, J. Phys. Soc. Jpn. **74**, 2169 (2005).
[44] T. Shigeoka, T. Morita, T. Fujiwara, K. Matsubayashi, and Y. Uwatoko, Phys. Proc. **75**, 845 (2015).
[45] T. Kong, W. R. Meier, Q. Lin, S. M. Saunders, S. L. Bud'ko, R. Flint, and P. C. Canfield, Phys. Rev. B **94**, 144434 (2016).
[46] K. Stevens, Proc. Phys. Soc. Sect. A **65**, 209 (1952).
[47] M. T. Hutchings, Solid State Phys. **16**, 227 (1964).
[48] D. Kaczorowski *et al.*, Intermetallics **19**, 964 (2011).
[49] S. Gupta, K. Suresh, A. Lukoyanov, Y. V. Knyazev, and Y. I. Kuz'min, J. Alloys Compd. **650**, 542 (2015).
[50] S. B. Gupta, K. Suresh, and A. Nigam, J. Appl. Phys. **112**, 103909 (2012).
[51] V. Burnett, D. Yazici, B. White, N. Dilley, A. Friedman, B. Brandom, and M. Maple, J. Solid State Chem. **215**, 114 (2014).
[52] N. H. Luong, J. Franse, and N. H. Hai, J. Magn. Magn. Mater. **224**, 30 (2001).
[53] D. Noakes and G. Shenoy, Phys. Lett. A **91**, 35 (1982).
[54] E. A. Popova, R. Klingeler, N. Tristan, B. Büchner, and A. N. Vasiliev, Phys. Rev. B **85**, 174402 (2012).
[55] A. Tari, *The Specific Heat of Matter at Low Temperatures* (Imperial College, London, 2003).
[56] J. M. Coey, *Magnetism and Magnetic Materials* (Cambridge University Press, Cambridge, 2010).
[57] M. Phejar, V. Paul-Boncour, and L. Bessais, Intermetallics **18**, 2301 (2010).
[58] R.-W. Li, J.-R. Sun, Q.-A. Li, T. Zhu, S.-Y. Zhang, and B.-G. Shen, J. Appl. Phys. **93**, 8092 (2003).
[59] E. M. Levin, K. A. Gschneidner, Jr., and V. K. Pecharsky, Phys. Rev. B **65**, 214427 (2002).
[60] Z. W. Ouyang, V. K. Pecharsky, K. A. Gschneidner, Jr., D. L. Schlagel, and T. A. Lograsso, Phys. Rev. B **74**, 024401 (2006).
[61] D. Gignoux and D. Schmitt, Phys. Rev. B **48**, 12682 (1993).
[62] P. Bak, Rep. Prog. Phys. **45**, 587 (1982).
[63] D. Gignoux and D. Schmitt, J. Magn. Magn. Mater. **129**, 53 (1994).
[64] D. Gignoux and D. Schmitt, J. Alloys Compd. **225**, 423 (1995).